Many-body model for the cooperative Jahn-Teller effect in crystals and its associated orbital ordering

Toraya Fernández-Ruiz [1] Inés Sánchez-Movellán,[1] Juan María García-Lastra,[2,*] Miguel Moreno,[1]
José Antonio Aramburu,[1] and Pablo García-Fernández [1]

[1]*Departamento de Ciencias de la Tierra y Física de la Materia Condensada, Universidad de Cantabria, Cantabria Campus Internacional,
Avenida de los Castros s/n, 39005 Santander, Spain*
[2]*Department of Energy Conversion and Storage, Technical University of Denmark, 2800 Kgs. Lyngby, Denmark*

In this work, we propose a many-body model for cooperative Jahn-Teller/orbital ordering in crystals containing unpaired electrons in locally degenerate e-shells ($KCuF_3$, CuO, $CuCl_2$, ...) that moves away from the usual Heisenberg-like expressions for solids and that is closely related to the usual local Jahn-Teller formulation for molecules and impurities. In particular, we show that the crystal problem can be expressed as a $[E_g(\Gamma) + E_g(R)] \otimes [e_g^{st}(\Gamma) + e_g^{ph}(R)]$ combined Jahn-Teller and pseudo-Jahn-Teller problem where the involved distortion modes $e_g^{st}(\Gamma)$ and $e_g^{ph}(R)$ are, respectively, a ferrodistortive strain mode and a phonon (ferro- or antiferrodistortive) mode that are strongly coupled among themselves. This model, fully consistent with experimental data, allows us to predict new phases that are separated by only a few meV from the ground state, and to propose ways to observe them. First-principles simulations fully support these findings. Comparison of our model with previous orbital ordering models shows subtle yet significant differences in the way orbital degrees of freedom work. We finally show that many orbital ordering models and density functional theory simulations yield solutions that are not consistent with Bloch's theorem and should be regarded with caution.

I. INTRODUCTION

In its inception, the Jahn-Teller effect [1] was intended to explain the distorted, low-symmetry geometrical configuration of molecules. However, as time passed, it started a field, associated with electron-vibration (vibronic) coupling, that first included other, nonmolecular localized systems like impurity sites in solids, and later evolved to cover many physical and chemical phenomena [2,3], including periodic solids [3–6]. The importance of vibronic coupling today can hardly be underestimated as it is the necessary tool to understand the shape of many molecules, as well as playing an important role in many phenomena ranging from spectroscopy [2] to colossal magnetoresistance [7] as well as having been the inspiration for the discovery of high-T_c superconductivity [8].

Nevertheless, the formulations of molecular and solid-state vibronic problems are currently quite different as the models for periodic systems, most notably the cooperative Jahn-Teller effect [3,6,9] and orbital ordering models [10–14], deviate from the original formulation and focus on describing interactions across the cells of a crystal, expressing them in a similar way to Heisenberg Hamiltonians. This seems justified since, for example, all *static* molecular Jahn-Teller problems associated with E_g degenerate states in octahedral configuration, like the one appearing when Cu^{2+} is placed in a perfect O_h complex as in the impurity centers $CaO:Ag^{2+}$ or $KZnF_3:Cu^{2+}$, lead to a tetragonally (D_{4h}) distorted AgO_6^{10-} or CuF_6^{4-} complex. On the other hand, the distortion of a

system that we could imagine as formed of a periodic array of perfectly octahedral CuF_6^{4-} complexes connected by the vertices, the $KCuF_3$ crystal, leads to orthorhombic distortions that alternate in an antiferrodistortive pattern. In this work, we try to formulate the problem of having such a lattice of active Jahn-Teller centers in a periodic solid as closely to the molecular $E_g \otimes e_g$ problem as possible. During this process, we will need to clearly differentiate between the consequences of the presence of various vibronic effects in crystals (Jahn-Teller effect versus pseudo-Jahn-Teller effect) as they lead to different physical outcomes and, on occasion, they are mixed up in the literature. On the practical side, we will verify our model using density functional theory (DFT) calculations, concentrating on a variety of crystals containing Cu^{2+} ions, that present various high-symmetry, parent [15] phases (perovskite, rocksalt, and hexagonal bidimensional) and where we will find that the models reveal similar patterns in all of them. We will demonstrate that this point of view brings to light oversights in previous models and allows predicting close-in-energy phases that could be stabilized, for example through strain engineering. Particular attention will be paid to the usual assumption in solid-state models where the bands formed by the degenerate orbitals are expected to be relatively narrow. This condition can be applied in the sense that local orbitals are relatively free to rotate at the cubic configuration, independently of what other nearby orbitals are doing. However, observing the e_g-bands calculated for $KCuF_3$ using DFT in Fig. 1, we can see that they span a range of almost 3 eV, which is clearly not negligible. It thus seems important to take into account, somehow, that the bands formed by the locally degenerate e_g orbitals are quite dispersive and
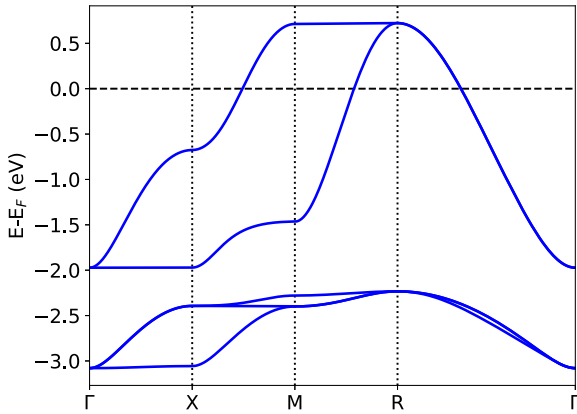
*garciapa@unican.es

FIG. 1. Bands with strong Cu($3d$) character when KCuF$_3$ is simulated using DFT forcing cubic symmetry. The lower three bands have d_{xy}, d_{xz}, and d_{yz} local character and correspond to the t_{2g} manifold. The upper two bands have d_{z^2}, $d_{x^2-y^2}$ local character and correspond with the e_g manifold. Note the much higher dispersion of the σ-bonding e_g bands when compared with the π-bonding t_{2g} ones.
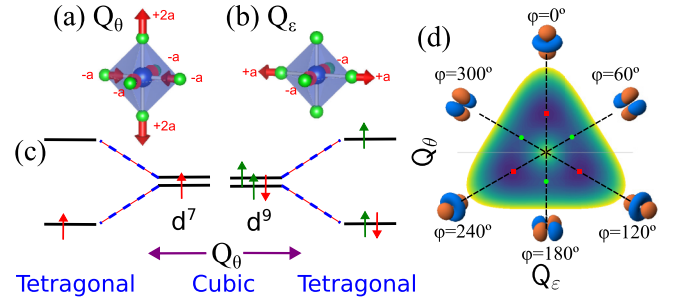

FIG. 2. Illustration of the main quantities involved in the Jahn-Teller effect on a d^7 or d^9 impurity in an octahedral environment. Parts (a) and (b) illustrate the tetragonal Q_θ and orthorhombic Q_ε components of the e_g mode of the complex. Part (c) illustrates the splitting of the e_g orbital with the distortion. The up/down arrows indicate the electrons that populate the e_g shell in both d^7 and d^9 cases. The red arrows denote the active Jahn-Teller electrons, while those in green denote the inactive ones. Finally, part (d) shows the energy surface (warped Mexican hat) in $(Q_\theta, Q_\varepsilon)$-space. The red squares denote the three equivalent tetragonal minima, while the green circles denote the three equivalent tetragonal transition states. The orbital plots show the change of the χ_- wave function of the active electron with the polar angle φ.

the way this influences the cooperative Jahn-Teller effect and orbital ordering. This will be a main goal of our work, where we will study in detail the wave function of the solid and reinterpreting orbital ordering, both based on superexchange [10–14] or electron-phonon coupling [14,16], in view of the complementary requirements of translational symmetry and band dispersion.

While magnetic interactions are often linked to the Jahn-Teller distortions in part of the literature [10–14], our simulations show that their influence on the final geometry and orbital state of the system is minor, in agreement with other recent calculations [17,18]. Thus, our present model focuses solely on the vibronic interactions. In a second stage, magnetic interactions and their coupling with vibrational ones could easily be introduced, following a similar recipe to the one used to describe K$_2$CuF$_4$ and similar layered lattices, where it was shown [17] that passing from antiferromagnetic to ferrocoupling slightly softened an antiferrodistortive phonon mode.

The manuscript is structured in three main sections. In the first one (Sec. II), we will describe the need to create a multielectron (many-body) model to describe vibronic effects in pure crystals. There, we will start by defining in some detail the degenerate state that gives rise to the Jahn-Teller effect in crystals, and we will continue by explaining the distortions that couple to this degenerate state and introducing the electron-nuclear coupling that leads to the vibronic coupling in these systems. We will show that the same Hamiltonian can be used to describe orbital ordering on the same footing. In the second part (Sec. III) we will provide the computational details for the DFT simulations that we have carried out to check that the predictions of our model are fully general and applicable to a large variety of situations. In the third section (Sec. IV) we perform DFT simulations for three different systems: (i) Tetragonal KCuF$_3$ that displays an antiferrotype orbital ordering and whose high-symmetry, parent structure is the Pm-$3m$ cubic perovskite KZnF$_3$, where Cu^{2+} complexes are connected by the vertices of the CuF$_6$

octahedra. (ii) CuO, whose orbital ordering is antiferrodistortive, like KCuF$_3$ but in contrast with the previous lattice displays monoclinic symmetry. In this case, the parent geometry is that of ZnO, a face-centered Fm-$3m$ cubic lattice. (iii) CuCl$_2$, a layered, van der Waals crystal where the distortions are ferrodistortive. In this case, we have simply simulated a single, almost bidimensional CuCl$_2$ layer whose parent structure, that of ZnCl$_2$, belongs to the hexagonal slab group Pm-31. Even though our DFT simulations are limited to systems containing Cu^{2+}, the model is perfectly applicable to other systems where the distortions can be attributed to the e_g-shell electronic structure like KCrF$_3$. Finally, in Sec. V we present our final conclusions.

II. MANY-BODY THEORY OF THE COOPERATIVE JAHN-TELLER EFFECT

The most usual formulation of the Jahn-Teller effect deals with localized systems like molecules and impurities in insulators, where typically the degenerate state is the result of the presence of an unpaired electron or hole inside a degenerate orbital. This is illustrated in Fig. 2 for the paradigmatic $E_g \otimes e_g$ problem, which is realized in, for example, d^7 or d^9 impurities in cubic lattices for systems like NaCl:Rh^{2+}, CaO:Cu^{2+}, or KZnF$_3$:Cu^{2+}, where one unpaired electron (or hole) occupies the e_g molecular orbital mainly associated with the d-shell of the metal [19–21]. When the octahedral complex centered around the metal distorts, following any combination of the vibrational modes that conform the e_g vibrational mode, the adiabatic energy is reduced and the resulting potential for the nuclei motion is the well-known warped Mexican hat [see Fig. 2(d)] [2,19]. The e_g mode is usually [2] described by the tetragonal Q_θ and the orthorhombic Q_ε coordinates that, in Van Vleck's notation [22], are denoted Q_3 and Q_2, respectively. In every single known low-spin d^7

or d^9 impurity, this energy surface presents three *tetragonal* equivalent minima and three *tetragonal* equivalent transition states that involve the elongation/compression of the complex along the x, y, or z directions, respectively. In these cases, the Jahn-Teller stabilization energy can be almost exclusively attributed to the orbital energy gained by the active electron, i.e., the electron that produces an occupation imbalance between the two degenerate orbitals (Fig. 2). In a perfect crystal, a coherent tunneling [23,24] among the three equivalent minima takes place. However, this situation is observed only in a few cases, such as Cu^{2+}-doped MgO or CaO, while usually coherence is destroyed by the unavoidable random strains leading to a local tetragonal symmetry and the so-called static Jahn-Teller effect [25,26]. Using polar coordinates to describe the e_g mode,

$$Q_\theta = \rho \cos \varphi, \qquad (1)$$

$$Q_\varepsilon = \rho \sin \varphi, \qquad (2)$$

the wave functions for the active electron ($-$) and hole ($+$) are, respectively,

$$|\chi_-(\varphi)\rangle = \cos \frac{\varphi}{2} |d_{z^2}\rangle - \sin \frac{\varphi}{2} |d_{x^2-y^2}\rangle, \qquad (3)$$

$$|\chi_+(\varphi)\rangle = \sin \frac{\varphi}{2} |d_{z^2}\rangle + \cos \frac{\varphi}{2} |d_{x^2-y^2}\rangle. \qquad (4)$$

A graphical depiction of the χ_- wave function with varying polar angle, φ, is shown in Fig. 2. While a large part of the literature on Cu^{2+} discusses the role of the unpaired hole in the e_g shell, here we will focus on the active Jahn-Teller electron (marked in red in Fig. 2), although it is important to note that both approaches are completely equivalent.

When moving from the localized Jahn-Teller problem to the crystal Jahn-Teller problem, the number of active electrons grows from 1 to one per site in the crystal, which is a very large number. In the same way, when considering the vibrations that can couple to an E_g state, in an impurity center these are usually limited to the local e_g mode of its ligands, but in a fully periodic solid there are many vibrational modes that couple to a degenerate state. In the Jahn-Teller bibliography [2] there are rigorous methods to deal with both multicenter and multimode Jahn-Teller problems, although these are not really practical with a crystal with an infinite number of centers and vibrational modes. To move beyond these approaches, some works, like those of Polinger [9,27], stress the importance of developing a deeper understanding of the effect of the band structure over the distortions occurring in solids. Our main goal in this work is to create a many-body model that allows us to describe the effect of the degeneracy in a solid with many active electrons that takes into account the band structure.

A first important observation is that the energy surface coming from first-principles methods on $KCuF_3$ or $LaMnO_3$ close to the cubic geometry shows a conical intersection where two many-body electronic states become degenerate (see, e.g., Refs. [15,28,29]), in full analogy to what happens in localized Jahn-Teller problems. This is a clear indication that in solids, as in impurities or molecules, there exists a ground degenerate E state. This is one of the main conclusions of orbital ordering models based on superexchange [10–14], as originally proposed by Kugel and Khomskii [11,12]. These

authors initially proposed [12] in 1973 that in the cubic phase $KCuF_3$ there are two many-body states where the hole wave function corresponds to alternating $x^2 - z^2/y^2 - z^2$ orbitals. This pattern has also been observed in DFT simulations in similar systems (see, e.g., Fig. 2 in Ref. [29]). However, as discussed in detail in Sec. IV A 1, we believe that this interpretation is not correct and is, in fact, due to a symmetry-broken solution resulting from limitations in the Kohn-Sham approach to DFT.

To establish the nature of the electronic ground state in a solid like $KCuF_3$, which includes a lattice of locally degenerate d^9 centers, we note that these systems ($KCuF_3$, CuO, ...) are insulators in their undoped ground state. This means that the wave function of the ground state can be written in terms of localized functions [30], i.e., Wannier orbitals. In particular, we can represent the wave function as a Slater determinant of the (infinite) Wannier functions, $\chi_{\vec{R}}$, that contain the active Jahn-Teller electron on each site. We will denote such a many-body wave function as

$$\Psi = |\ldots, \chi_{\vec{R}}, \ldots|, \qquad (5)$$

where the vertical bars represent the Slater determinant, and inside we consider the local wave functions associated with each of the electrons at the centers that are repeated periodically, as denoted by the ellipses ($\cdots$). In the considered problem, each of these Wannier functions will take the form of the $\chi_-(\varphi)$ orbital for each center [Eq. (3)], which we denote by $\chi_-(\varphi_{\vec{R}})$. So far this wave function is perfectly consistent with those obtained in orbital-ordering models [10–14,16] since the orbital angle can vary from center to center. However, according to the many-body Bloch theorem [31] (where $\vec{K}$ is the total momentum of all the electrons),

$$\Psi_{j\vec{K}}(\vec{r}_1 + \vec{R}, \vec{r}_2 + \vec{R}, \ldots) = e^{i\vec{K}\vec{R}} \Psi_{j\vec{K}}(\vec{r}_1, \vec{r}_2, \ldots) \qquad (6)$$

in a cubic lattice like the *Pm*-3*m* structure of a perovskite, the parent phase of $KCuF_3$, the *Fm*-3*m* structure of a rocksalt crystal, or like the high-symmetry configuration of CuO, all transition-metal sites should display the same density, i.e., the Wannier function associated with each site should be the same, with the exception of a phase factor. This means that, in cubic symmetry, one of the two states that become degenerate in the ground state of a solid is characterized by the orbital function χ_- in all its sites, while the other is characterized by having the χ_+ orbital function in all its sites. If we choose $\varphi_{\vec{R}} = 0$, that means that the d_{z^2} function becomes occupied in one many-body state while in the other the occupied orbital is $d_{x^2-y^2}$. Thus, using the generalized Bloch theorem, we can characterize the two many-body states that form the degenerate ground state in a lattice that contains many local Jahn-Teller active sites. As a result of the application of this theorem, we can state that the orbital ordering in the cubic geometry of a solid is not antiferrodistortive, as expected from models like Kugel-Khomskii, since those solutions show broken symmetry. This result does not rule out the possible importance of superexchange in the stabilization energy of the final, low-symmetry configuration, but it clearly shows that magnetism only plays a role after the geometry of the system has been distorted away from the cubic configuration. For more information, check Sec. IV A 1.
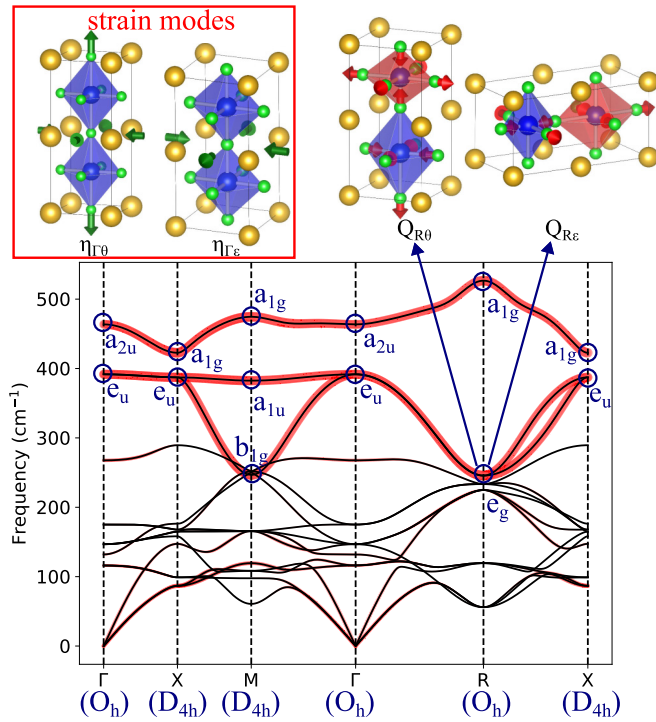
FIG. 3. Phonon dispersion diagram for KZnF$_3$ illustrative of crystals with perovskite parent structure like KCuF$_3$. The little group of reciprocal space points with inversion is indicated in blue. The intensity of the contribution of the Zn-F stretching to the vibration is marked in red. The antiferrodistortive e_g-phonon mode at R and the ferrodistortive strain e_g modes are shown at the top of the figure. The potassium, zinc, and fluorine ions are represented, respectively, by yellow, blue, and green spheres.

A. Vibrational and strain modes

After we have defined the degenerate ground electronic state in a crystal containing a lattice of active e_g-type Jahn-Teller sites, we need to find the vibrational states that couple to them. In cubic symmetry, E_g states can couple through e_g vibrational modes, giving rise to the $E_g \otimes e_g$ Jahn-Teller problem [2]. Here we will argue that these are the main modes through which the Jahn-Teller effect manifests in a solid. However, in solids there are vibrations, associated with points in reciprocal space whose little group is not cubic (different from O_h, see Fig. 3), that couple to the degenerate state, although their coupling strength will typically be smaller than those vibrations in points with cubic symmetry. The strength of the vibronic coupling between the E_g state with vibrations will depend on two main factors: (i) In systems with inversion symmetry, the Jahn-Teller effect can only occur through vibrations that have even symmetry. In a solid with cubic symmetry, phonons will only have well-defined parity on particular points of reciprocal space. This does not mean that Jahn-Teller coupling will only take place with vibrations at those points, but that the electron-vibration interaction integrals will be largest in absolute value for even modes (or exactly zero for odd ones) at them. (ii) We expect the important vibrational modes to contain a large contribution from the ligands that are the first neighbors of the active transition metals, as typically in the $E_g \otimes e_g$ Jahn-Teller effect in impurities

in octahedral sites these atoms are the main ones involved in the distortion. In the same way, we would expect these modes to involve the stretching of the metal-ligand bonds.

Let us first focus on crystals that come from the perovskite structure, like KCuF$_3$, although later we will discuss the cases of rocksalt (CuO) or hexagonal (CuCl$_2$) lattices in Secs. IV B and IV C, respectively. To discuss the symmetry of phonon modes, we will study KZnF$_3$, a cubic lattice that is the parent structure of KCuF$_3$ (the ionic radius [32] of Cu^{2+}, $r_{Cu} = 0.73$ Å, is analogous to that of Zn^{2+}, $r_{Zn} = 0.74$ Å), where the electronic degeneracy has been suppressed due to the closed-shell nature of the Zn^{2+} ions. Figure 3 shows the DFT-calculated phonon dispersion diagram for KZnF$_3$ showing the contribution of the metal-ligand stretch to each band in red. We can observe that the top three bands clearly show the largest stretching contribution. We can see that vibrations at Γ, X, M, and R show inversion symmetry, although only the little groups at Γ and R display full cubic (O_h) symmetry. The zone-center vibrations in Γ are all ferrodistortive and odd (*ungerade*) so they present no coupling. As we move to the border-zone along the different directions in reciprocal space, the modes become antiferrodistortive and even (*gerade*) so they begin coupling with the E_g electronic state in one dimension (X), two dimensions (M), and three dimensions (R). In this last point, we find the only O_h e_g-mode in the whole diagram, which is antiferrodistortive. The components of this mode, that we denote as $Q_{R\theta}$ and $Q_{R\varepsilon}$, are very important in the vibronic problems of this crystal. As shown in Fig. 3, both of them are antiferrodistortive, although $Q_{R\theta}$, related to the tetragonal mode Q_θ (Q_3), produces an alternating elongation/compression in neighboring transition-metal complexes while $Q_{R\varepsilon}$, related to the orthorhombic mode Q_ε (Q_2), produces an alternating orthorhombic distortion along the x/y directions. Most cooperative Jahn-Teller [3,9]/orbital ordering models [14,16] based on electron-phonon interactions involve $Q_{R\varepsilon}$ as the main distortion in perovskite-type crystals. As we will show in Sec. IV A, there are many interesting features of the energy surface of these systems associated with $Q_{R\theta}$ that have been overlooked by most of the literature.

Besides the antiferrodistortive modes, Kanamori [4] stressed the existence of Jahn-Teller active ferrodistortive modes associated with homogeneous strain modes. Many early works on the Jahn-Teller effect in solids [4–6,33] highlighted the importance of homogeneous strain too, although later electron-phonon models [9,16] tend to neglect their effect. There are two symmetrized strain modes (see, e.g., Ref. [26]) that transform as e_g (see Fig. 3). Given that these strain modes alter all sites in the lattice in the same way, they are associated with the Γ point in reciprocal space. Similarly to the phonon modes (see Fig. 3), these strain components can be written as a tetragonal, $\eta_{\Gamma\theta}$, and an orthorhombic, $\eta_{\Gamma\varepsilon}$, mode.

As in the case of the local e_g-coordinates, Eqs. (1) and (2), it will be useful to express the crystal distortions in terms of polar coordinates:

$$\eta_{\Gamma\theta} = \eta_\Gamma \cos\varphi_\Gamma, \quad \eta_{\Gamma\varepsilon} = \eta_\Gamma \sin\varphi_\Gamma; \quad (7)$$

$$Q_{R\theta} = Q_R \cos\varphi_R, \quad Q_{\Gamma\varepsilon} = Q_R \sin\varphi_R. \quad (8)$$

To finish this section, we would like to remark that the existence [34] of A- (most common) and D-type (less common) polytypes of KCuF$_3$ can be directly traced to the stabilization of the system along $Q_{R\varepsilon}$ or $Q_{Mb_{1g}}$ modes. The b_{1g} mode (see Fig. 3) is closely related to $Q_{R\varepsilon}$ and is associated with the splitting of the e_g mode. However, since it is not a cubic mode, its total coupling to E_g is somewhat weaker than the mode at R leading to a less stable structure.

B. The model Hamiltonian

Now that we have selected the vibrations that can participate in the vibronic problem, we will follow the usual procedure [2,19] and expand the Hamiltonian operator with the distortions. In this approach, we will retain linear vibronic operators ($\hat{H}_{\text{vib}}$) and also include elastic harmonic ($\hat{H}_{\text{harm}}$) and third-order anharmonic terms ($\hat{H}_{\text{anharm}}$),

$$\hat{H} = \hat{H}_0 + \hat{H}_{\text{vib}} + \hat{H}_{\text{harm}} + \hat{H}_{\text{anharm}}, \qquad (9)$$

as first-principles calculations for impurities and molecules [19] showed these interactions were the most important in Jahn-Teller problems. In the above expression, $\hat{H}_0$ is the electronic Hamiltonian for the cubic phase, and the vibronic and harmonic terms take their usual expressions,

$$\hat{H}_{\text{vib}} = \frac{\partial \hat{H}}{\partial \eta_{\Gamma\theta}}\eta_{\Gamma\theta} + \frac{\partial \hat{H}}{\partial \eta_{\Gamma\varepsilon}}\eta_{\Gamma\varepsilon} + \frac{\partial \hat{H}}{\partial Q_{R\theta}}Q_{R\theta} + \frac{\partial \hat{H}}{\partial Q_{R\varepsilon}}Q_{R\varepsilon} \quad (10)$$

and

$$\hat{H}_{\text{harm}} = \tfrac{1}{2}C_\eta\big(\eta_{\Gamma\theta}^2 + \eta_{\Gamma\varepsilon}^2\big) + \tfrac{1}{2}K_R\big(Q_{R\theta}^2 + Q_{R\varepsilon}^2\big), \qquad (11)$$

where C_η and K_R are, respectively, the elastic coefficient for the tetragonal strains and the force constant for the e_g-mode at R. To obtain the anharmonic cubic elastic interactions, obtained as a triple-product of coordinates that transforms like the totally symmetric representation [19] (that in periodic solids is the combined a_{1g} associated with the point-group operations and Γ with respect to translations), we notice some important differences between the antiferrodistortive phonon modes ($Q_{R\varepsilon}$) and the ferrodistortive strain modes. While the strain modes can be directly combined to form a cubic term that is equivalent to the one proposed by Öpik and Pryce [35] to explain why most octahedral Jahn-Teller complexes are elongated ($C_{3\eta} < 0$),

$$\hat{H}_{3\eta} = C_{3\eta}\big(\eta_{\Gamma\theta}^3 - 3\eta_{\Gamma\varepsilon}^2\eta_{\Gamma\theta}\big), \qquad (12)$$

it is not possible to do the same for the phonon modes at R. The reason behind this is that the product of three coordinates involving the R-point of the reciprocal lattice transforms as a quantity in R and thus it is not totally symmetric (that transforms as Γ). Thus, we see that the antiferrodistortive e_g-mode at R behaves quite differently from a usual Jahn-Teller coordinate. However, using Clebsch-Gordan coefficients [36], it is possible to obtain an Öpik and Pryce [35]-like term that involves a cross-product of quadratic Q_R phonon-modes and linear η_Γ strain-modes,

$$\hat{H}_{3Q\eta} = V_{3Q\eta}\frac{1}{\sqrt{2}}\big[\eta_{\Gamma\theta}\big(Q_{R\varepsilon}^2 - Q_{R\theta}^2\big) + \eta_{\Gamma\varepsilon}2Q_{R\theta}Q_{R\varepsilon}\big]. \quad (13)$$

As $\eta_{\Gamma\theta} > 0$ decreases (increases) the in-plane (axial) distances, which should soften the axial $Q_{R\theta}$ mode and harden the in-plane $Q_{R\varepsilon}$ one, $V_{3Q\eta}$ has to be positive.

We can now build the Jahn-Teller Hamiltonian matrix using the low-energy eigenstates of H_0,

$$H_{ij} = \langle \Psi_i | \hat{H} | \Psi_j \rangle, \qquad (14)$$

although we immediately notice that the antiferrodistortive phonon-mode coordinates yield null vibronic constants,

$$\langle \Psi_i | \frac{\partial \hat{H}}{\partial Q_{R\theta}} | \Psi_j \rangle = \langle \Psi_i | \frac{\partial \hat{H}}{\partial Q_{R\varepsilon}} | \Psi_j \rangle = 0. \qquad (15)$$

The underlying cause is the fact that, as we defined them above, the functions Ψ_i and Ψ_j belong to the same point in reciprocal space [37]. Thus, the expected value of an operator that transforms as R is zero, as the integral does not fulfill Bragg's law [38] $(\vec{k}_i - \vec{k}_j + \vec{q}_R = \vec{G})$, so the difference between the wave vectors of the i and j wave functions plus the wave vector of the vibration must be a reciprocal-lattice vector, $\vec{G}$. However the experimental geometry of KCuF$_3$ clearly shows that the Q_R phonon modes are important in these systems. This means that in the model for these systems, we need to involve many-body wave functions transforming like E but separated from each other by a vector $(\frac{1}{2}, \frac{1}{2}, \frac{1}{2})$ of the reciprocal lattice. Given that the only points of reciprocal space where cubic symmetry (O_h little group) exists are Γ and R, we will evaluate the vibronic Hamiltonian with E_Γ ($\Psi_{\Gamma\theta}$, $\Psi_{\Gamma\varepsilon}$) and E_R ($\Psi_{R\theta}$, $\Psi_{R\varepsilon}$) wave functions. As these two states are at different points of reciprocal space, they will have different energies (see Fig. 1 for one-electron bands),

$$\langle \Psi_{\Gamma\theta} | \hat{H}_0 | \Psi_{\Gamma\theta} \rangle = \langle \Psi_{\Gamma\varepsilon} | \hat{H}_0 | \Psi_{\Gamma\varepsilon} \rangle = -\Delta/2, \qquad (16)$$

$$\langle \Psi_{R\theta} | \hat{H}_0 | \Psi_{R\theta} \rangle = \langle \Psi_{R\varepsilon} | \hat{H}_0 | \Psi_{R\varepsilon} \rangle = \Delta/2 \qquad (17)$$

showing that the Jahn-Teller problem in solids is a combination of Jahn-Teller and pseudo-Jahn-Teller effects. This distinction is important, as in the Jahn-Teller effect the adiabatic energy surface *always* presents low-symmetry equilibrium points, while in the pseudo-Jahn-Teller effect the instability condition [2], $K_0 + K_v < 0$, needs to be fulfilled, i.e., the vibronic coupling constant F, participating in the vibronic contribution ($K_v = -F^2/\Delta$), needs to be larger than the positive [2] primary force constant, K_0, to produce a distortion. This means that the strain distortion always produces a distortion (it represents a force that distorts the system) while the antiferrodistortive Q_R phonon may not (depending on the instability condition). Thus, the strain mode is *necessary* and should always be considered. The linear vibronic constants are

$$F_{\Gamma\Gamma,\Gamma} = -\langle \Psi_{\Gamma\theta} | \frac{\partial \hat{H}}{\partial \eta_{\Gamma\theta}} | \Psi_{\Gamma\theta} \rangle = \langle \Psi_{\Gamma\varepsilon} | \frac{\partial \hat{H}}{\partial \eta_{\Gamma\theta}} | \Psi_{\Gamma\varepsilon} \rangle$$

$$= \langle \Psi_{\Gamma\theta} | \frac{\partial \hat{H}}{\partial \eta_{\Gamma\varepsilon}} | \Psi_{\Gamma\varepsilon} \rangle = \langle \Psi_{\Gamma\varepsilon} | \frac{\partial \hat{H}}{\partial \eta_{\Gamma\varepsilon}} | \Psi_{\Gamma\theta} \rangle, \qquad (18)$$

$$F_{RR,\Gamma} = -\langle \Psi_{R\theta} | \frac{\partial \hat{H}}{\partial \eta_{\Gamma\theta}} | \Psi_{R\theta} \rangle = \langle \Psi_{R\varepsilon} | \frac{\partial \hat{H}}{\partial \eta_{\Gamma\theta}} | \Psi_{R\varepsilon} \rangle$$

$$= \langle \Psi_{R\theta} | \frac{\partial \hat{H}}{\partial \eta_{\Gamma\varepsilon}} | \Psi_{R\varepsilon} \rangle = \langle \Psi_{R\varepsilon} | \frac{\partial \hat{H}}{\partial \eta_{\Gamma\varepsilon}} | \Psi_{R\theta} \rangle, \qquad (19)$$

$$F_{\Gamma R,R} = -\langle\Psi_{\Gamma\theta}|\frac{\partial\hat{H}}{\partial Q_{R\theta}}|\Psi_{R\theta}\rangle = \langle\Psi_{\Gamma\varepsilon}|\frac{\partial\hat{H}}{\partial Q_{R\theta}}|\Psi_{R\varepsilon}\rangle$$

$$= \langle\Psi_{\Gamma\theta}|\frac{\partial\hat{H}}{\partial Q_{R\varepsilon}}|\Psi_{R\varepsilon}\rangle = \langle\Psi_{\Gamma\varepsilon}|\frac{\partial\hat{H}}{\partial Q_{R\varepsilon}}|\Psi_{R\theta}\rangle. \tag{20}$$

Considering that the main part of the vibronic constants will come from the local coupling between the e_g orbitals in each

of the centers and the e_g distortion of the complex of the metal and its first neighbors, we can approximate

$$F = F_{\Gamma\Gamma,\Gamma} \approx -F_{RR,\Gamma} \approx -F_{\Gamma R,R}, \tag{21}$$

where the change of sign comes from the phase change of going from one center to the next one in R wave functions. Within this approximation, the Jahn-Teller Hamiltonian matrix is

$$\hat{H}_{\text{eff}} = \begin{pmatrix} -\Delta/2 - F\eta_{\Gamma\theta} & F\eta_{\Gamma\varepsilon} & FQ_{R\theta} & -FQ_{R\varepsilon} \\ F\eta_{\Gamma\varepsilon} & -\Delta/2 + F\eta_{\Gamma\theta} & -FQ_{R\theta} & -FQ_{R\varepsilon} \\ FQ_{R\varepsilon} & -FQ_{R\theta} & \Delta/2 + F\eta_{\Gamma\theta} & -F\eta_{\Gamma\varepsilon} \\ -FQ_{R\theta} & -FQ_{R\varepsilon} & -F\eta_{\Gamma\varepsilon} & \Delta/2 - F\eta_{\Gamma\theta} \end{pmatrix} + \frac{1}{2}C_\eta(\eta_{\Gamma\theta}^2 + \eta_{\Gamma\varepsilon}^2) + \frac{1}{2}K_R(Q_{R\theta}^2 + Q_{R\varepsilon}^2)$$

$$+ C_{3\eta}(\eta_{\Gamma\theta}^3 - 3\eta_{\Gamma\varepsilon}^2\eta_{\Gamma\theta}) + V_{3Q\eta}\frac{1}{\sqrt{2}}[\eta_{\Gamma\theta}(Q_{R\varepsilon}^2 - Q_{R\theta}^2) + \eta_{\Gamma\varepsilon}2Q_{R\theta}Q_{R\varepsilon}]. \tag{22}$$

Let us now discuss the shape of the adiabatic potential energy surface (APES) described by Eq. (22). We will start by studying what happens for the η_Γ and Q_R modes individually. In the first case (making $Q_R = 0$) we can plot the APES cross-section with $\eta_{\Gamma\theta}$, which describes the energy of the system under a (ferroelastic) simultaneous elongation ($\eta_{\Gamma\theta} > 0$)/compression ($\eta_{\Gamma\theta} < 0$) of all CuF_6^{4-} octahedra in the $KCuF_3$ lattice [see Fig. 4(a)]. We can observe that the energy surface corresponds with the typical plot for a Jahn-Teller effect in a molecule both for the lower E-state (red and blue lines around $\eta_\theta = 0$) and the higher E-state (green and yellow lines around $\eta_\theta = 0$) where the two lower minima corresponding to elongated and compressed octahedra appear at different energies due to the action of the Öpik and Pryce [35] cubic term [Eq. (12)]. When we study the energy surface on the full $\eta_{\Gamma\theta}/\eta_{\Gamma\varepsilon}$ space [Fig. 4(b)], we observe the usual warped Mexican hat where the minima/saddle points correspond to tetragonal symmetry, which in the case of $KCuF_3$ belongs to the $P4/mmm$ (D_{4h}) space group without the presence of the orthorhombic minima characteristic of the cooperative Jahn-Teller effect and orbital ordering models.

In the second case, making $\eta_\Gamma = 0$, we can plot the APES cross-section with $Q_{R\theta}$ [see Fig. 4(c)], which describes the antiferroelastic distortion where the octahedra compress/elongate alternatively along the 3-Cartesian axes (as illustrated in Fig. 3). This distortion mixes the many-electron wave functions at Γ and R that have different energies [the $(E + E') \otimes e$ pseudo-Jahn-Teller problem [2]] and so the degeneracy is maintained but the lower sheet displays a negative curvature, in contrast with the conical intersection shown for the η_Γ coordinate. Calculation of the lower-energy surface in the $Q_{R\theta}/Q_{R\varepsilon}$ space is fully consistent with the $(E + E) \otimes e$ pseudo-Jahn-Teller problem in molecules, where, using as a first approximation just linear coupling, we obtain a circular trough [Fig. 4(d)].

After observing the energy surfaces of the η_Γ and Q_R distortion modes individually, let us now discuss their interplay. In a first approximation, we will neglect the cubic coupling term between these modes [Eq. (13)]. The ground energy surface in the $\eta_{\Gamma\theta}/Q_{R\theta}$ and $\eta_{\Gamma\theta}/Q_{R\varepsilon}$ cross-sections is represented

in Figs. 5(a) and 5(b). In the first one, we can observe that the deepest energy wells correspond with the pure Jahn-Teller (η_Γ coordinate, $Q_R = 0$) minima, and no significant interaction occurs between the modes. However, when the surface is represented in the $\eta_\theta/Q_{R\varepsilon}$ coordinates, four equivalent global minima appear (these are represented for the tetragonal strain along z but there are eight more minima following the strains along x and y, as corresponds with cubic symmetry). Each of these minima involves a combination of a global elongation ($\eta_{\Gamma\theta} > 0$) or compression ($\eta_{\Gamma\theta} < 0$) of all the octahedral complexes of the crystal along the z-axis with an antiferrodistortive checkerboard patterned orthorhombic distortion where neighboring octahedra have elongated/shortened bonds with their ligands in the x and y directions.

The experimental (and first-principles calculated) geometry of $KCuF_3$ involves a simultaneous ferroelastic compression of all octahedra, which is often neglected in models, with the antiferrodistortive orthorhombic distortion in the xy-plane represented by the lower two minima in Fig. 5(b). This asymmetry in the energy surface can be described by the elastic coupling of Eq. (13). When this term is considered, the energy surfaces of Figs. 5(c) and 5(d) emerge. Under this term, the compression of all the octahedral complexes of the solid due to $\eta_{\Gamma\theta} < 0$ has the physical effect of reducing the hardness of the orthorhombic in-plane distortion $Q_{R\varepsilon}$ as the distance between the metal and its in-plane ligands is increased. We would like to remark here that compressed complexes are relatively common in layered systems [17,39]. This, in turn, favors a stronger pseudo-Jahn-Teller effect as the effective elastic force constant (K_R) is reduced. On the other hand, for the elongated minima the in-plane metal-ligand distance is reduced and the K_R force constant increases hindering the effect of the pseudo-Jahn-Teller effect and making the energy associated with those minima increase. It is important to note that while in Fig. 5(d) this effect is moderate, as the chosen $V_{3Q\eta}$ is relatively small (0.1) with regard to the chosen F and K values (1 in arbitrary units), in first-principles simulations the effect of this coupling is very large and is one of the dominant effects on the shape of the energy surface. Another very important note is that, contrary to Kanamori's model for
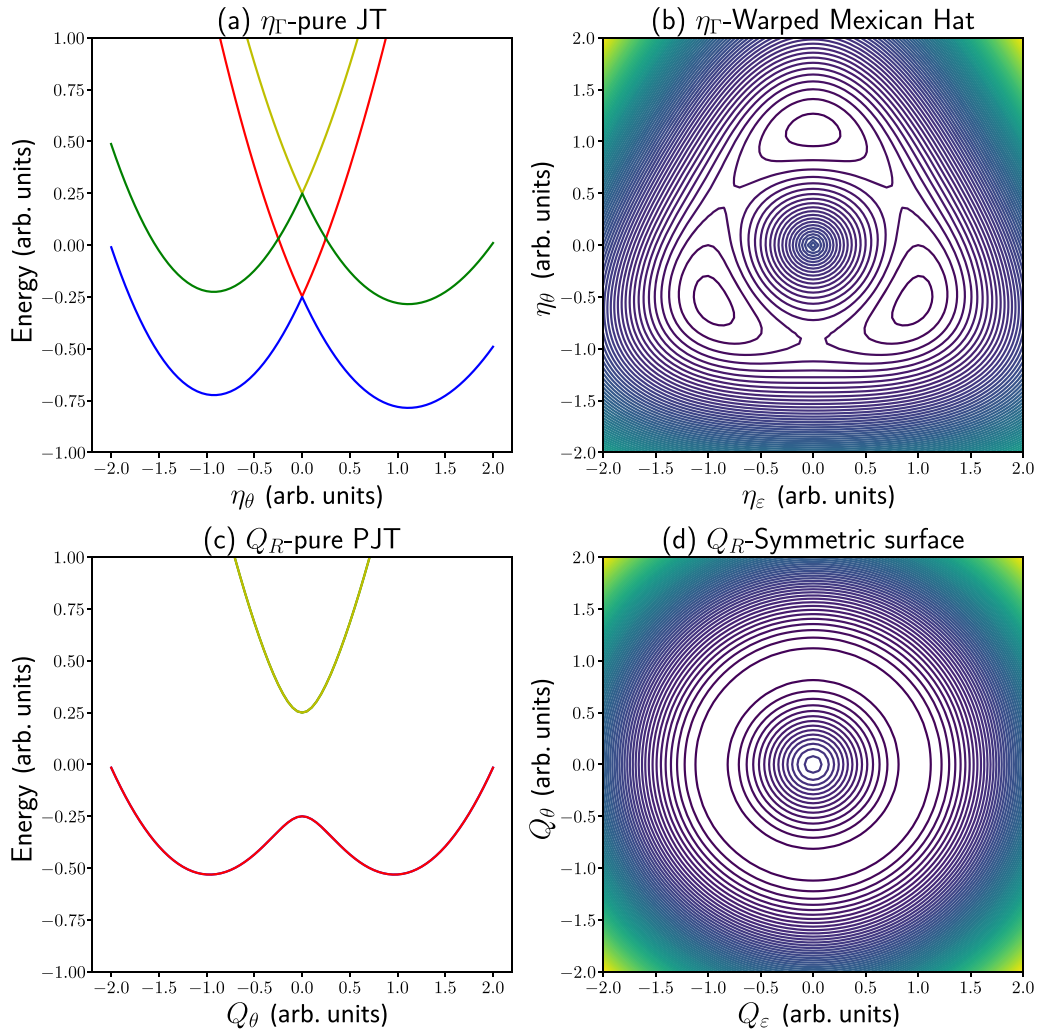
FIG. 4. Adiabatic potential energy surfaces associated with the vibronic Hamiltonian for the individual η_Γ and Q_R distortions. In (a) we show the energy cross-section along the ferroelastic tetragonal distortion of the whole solid, $\eta_{\Gamma\theta}$, showing the conical intersection for the degenerate states at Γ and R. In (b) we show the energy of the ground state in the $(\eta_{\Gamma\theta}, \eta_{\Gamma\varepsilon})$ coordinates as a contour plot showing the usual Mexican hat-shape of a Jahn-Teller effect. In (c) the energy cross-section is shown for the $Q_{R\theta}$ mode and in (d) the contour plot is shown for the ground state in the $(Q_{R\theta}, Q_{R\varepsilon})$ coordinates. The parameters used to obtain these plots are, in arbitrary units, $\Delta = 0.5$, $F = 1.0$, $K_R = 1.0$, $C_\eta = 1.0$, $C_{3\eta} = 0.1$, $V_{3Q\eta} = -0.03$.

the cooperative Jahn-Teller effect [4], the ferrodistortive and antiferrodistortive distortions in a solid are not competitive but cooperative with each other.

The effect described above is not the only consequence of considering the cubic term of Eq. (13). In Fig. 5(c) we can see that it also increases the depth of the $\eta_\theta/Q_{R\theta}$ top well, creating, in fact, two minima that combine $\eta_\theta > 0$ and $Q_{R\theta} \neq 0$. This geometry involves a global elongation of the complexes combined with an alternative further elongation/compression of neighboring Jahn-Teller complexes, a solution that comes out in some orbital-ordering models [16]. The physical phenomenon is similar to the one in play for the $\eta_{\Gamma\theta}/Q_{R\varepsilon}$ cooperation. The $\eta_{\Gamma\theta}$ mode increases the distance in the axis, which, in turn, softens the K_R force constant along the $Q_{R\theta}$ distortion, favoring the realization of this pseudo-Jahn-Teller distortion. This phase, to our knowledge, has never been observed but both our model and our first-principles simulations (Sec. IV A) point towards its existence.

In the following section, we discuss the consequences that our model has with respect to the ordering of the orbitals inside the crystal.

C. Orbital ordering

To calculate the orbital ordering, we will employ the vibronic Hamiltonian of Eq. (9) and a variational trial function. As indicated above, crystals with the cooperative Jahn-Teller effect like $KCuF_3$, CuO, etc. are insulators, and so their wave function can be approximated with the use of a Slater determinant for the active electrons whose wave functions are described by Eq. (3), the local (Wannier) functions $\chi_-(\varphi_{\bar{R}})$. To create the degrees of freedom necessary to allow for orbitals coupled in a ferro or antiferro manner, we will take a supercell that contains two Jahn-Teller centers that we will name 1 and 2, i.e., in $KCuF_3$ we would take a supercell that contains two Cu ions. The local orbital in center 1 will be described by
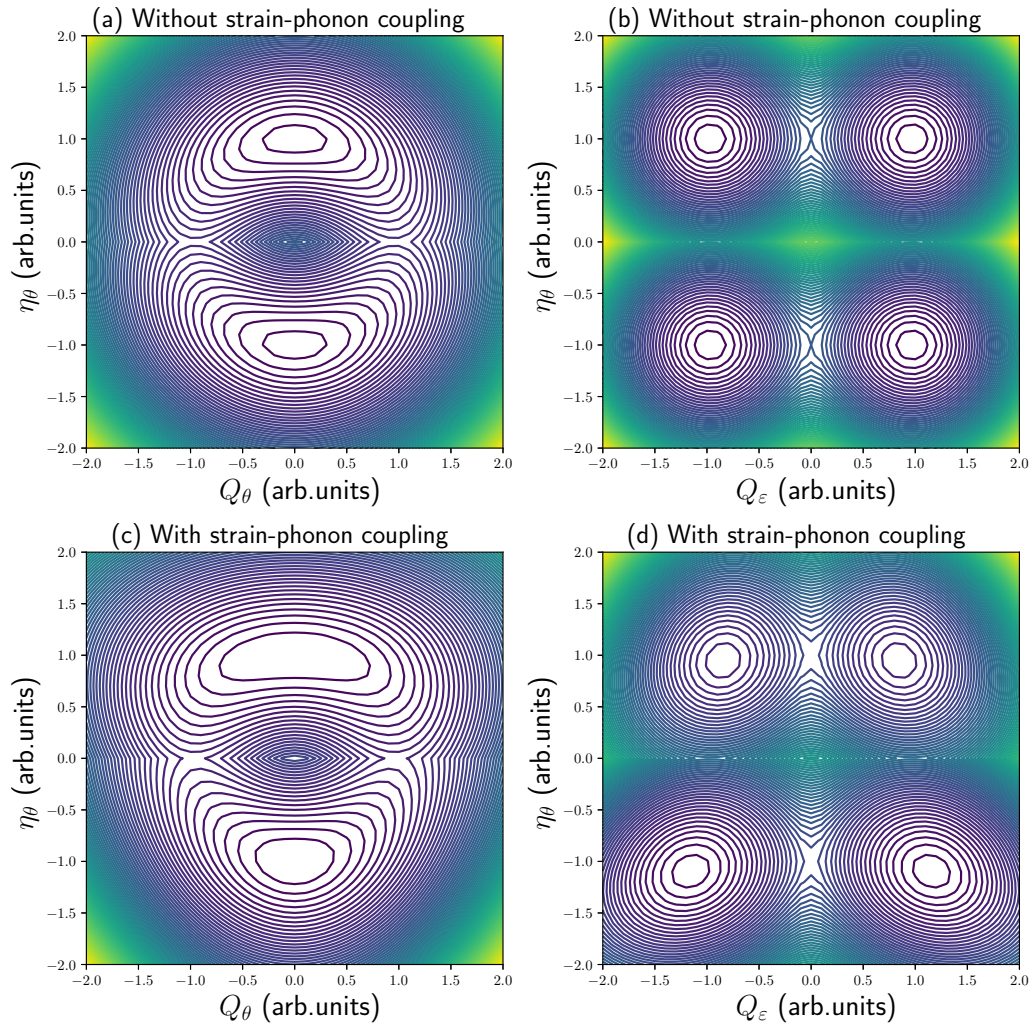
FIG. 5. Contour plots of the ground state associated with the vibronic Hamiltonian illustrating the coupling of η_Γ and Q_R distortions. In panels (a) and (c) the energy along the tetragonal strain mode, $\eta_{\Gamma\theta}$, and the alternating elongated/compressed mode, $Q_{R\theta}$, is shown. A similar representation is done in panels (b) and (d) using the $\eta_{\Gamma\theta}$ and the orthorhombic antiferrodistortive mode, $Q_{R\varepsilon}$, instead. In the top (a) and (b) panels, the intermode coupling is not considered while in (c) and (d) it takes a non-null value, otherwise all parameters are the same as in Fig. 4.

the orbital angle φ_1, and with the respective angle (φ_2) for the second center. Under these approximations, the ground-state wave function can be written as

$$\Psi_- = |\ldots, \chi_-(\varphi_1), \chi_-(\varphi_2), \ldots, |, \qquad (23)$$

where we followed the notation used in Eq. (5) using a two-center supercell as a basic repetition unit to create the crystal. The orbital ordering can be obtained by evaluating the Hamiltonian, Eq. (9), and then minimizing its energy with respect to φ_1 and φ_2.

To simplify the solution, we will write the orbital angles as a combination of an angle that will account for ferrotype orbital ordering, φ_f, and another that will describe antiferrotype orbital ordering, φ_a,

$$\varphi_1 = \varphi_f + \varphi_a, \qquad (24)$$

$$\varphi_2 = \varphi_f - \varphi_a. \qquad (25)$$

Moreover, due to the coupling of the electronic states through the R-point e_g-phonon mode, when the coordinates $Q_{R\theta}$ or $Q_{R\varepsilon}$ are not null, the orbitals will display a superposition of two components that transform like functions at Γ and R, respectively. Rendering this admixture in real space requires doubling the cell used to represent the wave function, as laid down in Eq. (23). This clearly shows the connection of the pseudo-Jahn-Teller effect through vibrations at the border of the Brillouin zone with the Peierls effect [40], where a symmetry-lowering *dimerization* occurs in a linear chain when wave functions at Γ and X are allowed to mix. The Γ component (χ_Γ) must be common to both the $\chi_-(\varphi_1)$ and $\chi_-(\varphi_2)$ orbitals, and it needs to be related to its sum,

$$\frac{\chi_-(\varphi_1) + \chi_-(\varphi_2)}{2} = \cos\frac{\varphi_a}{2}\chi_-(\varphi_f) = \cos\frac{\varphi_a}{2}\chi_\Gamma \qquad (26)$$

while their difference must contain the R contribution (χ_R),

$$\frac{\chi_-(\varphi_1) - \chi_-(\varphi_2)}{2} = -\sin\frac{\varphi_a}{2}\chi_+(\varphi_f) = -\sin\frac{\varphi_a}{2}\chi_R. \qquad (27)$$

Thus,

$$\chi_-(\varphi_1) = \cos\frac{\varphi_a}{2}\chi_\Gamma - \sin\frac{\varphi_a}{2}\chi_R, \tag{28}$$

$$\chi_-(\varphi_2) = \cos\frac{\varphi_a}{2}\chi_\Gamma + \sin\frac{\varphi_a}{2}\chi_R. \tag{29}$$

These wave functions change sign when φ_a or φ_f changes by 2π, showing a more complex pattern for the Berry phase [41] than the one commonly found in localized Jahn-Teller problems [42].

The application of the cubic Hamiltonian, $\hat{H}_0$, over the wave function at Γ and R, Eqs. (16) and (17), yields a gap Δ. Hence we can now use Eqs. (28) and (29) to evaluate the energy of the Slater determinant, Eq. (23), with the vibronic Hamiltonian, Eq. (9). The result, obtained taking into account that the local distortion in each of the centers is the same for η_Γ and the opposite for Q_R [Eqs. (7) and (8)], is

$$\begin{aligned}
E = &-\frac{\Delta}{2}\cos\varphi_a + H_{\text{harm}} + H_{\text{anharm}} \\
&- F\eta_\Gamma\cos\varphi_a(\cos\varphi_f\cos\varphi_\Gamma + \sin\varphi_f\sin\varphi_\Gamma) \\
&- FQ_R\sin\varphi_a(-\sin\varphi_f\cos\varphi_R + \cos\varphi_f\sin\varphi_R).
\end{aligned} \tag{30}$$

To obtain the ground-state energy using this expression, we need to input the geometry, given by the η_Γ and Q_R modes, and then use the variational principle ($\partial E/\partial\varphi_f = 0$, $\partial E/\partial\varphi_a = 0$) to obtain the value of the orbital angles. In other words, the orbital angles are given by the expressions

$$\tan\varphi_f = \frac{-\eta_\Gamma\cos\varphi_a\sin\varphi_\Gamma + Q_R\sin\varphi_a\cos\varphi_R}{\eta_\Gamma\cos\varphi_a\cos\varphi_\Gamma + Q_R\sin\varphi_a\sin\varphi_R}, \tag{31}$$

$$\tan\varphi_a = \frac{FQ_R(-\sin\varphi_f\cos\varphi_R + \cos\varphi_f\sin\varphi_R)}{\Delta/2 + 2F\eta_\Gamma(\cos\varphi_f\cos\varphi_\Gamma + \sin\varphi_f\sin\varphi_\Gamma)}, \tag{32}$$

where we see that the solutions for φ_f and φ_a ordering are closely entangled, leading to nontrivial orbital orderings.

Using Eqs. (31) and (32), it is easy to show that if $Q_R = 0$, the minimum implies $\varphi_a = 0$, i.e., under a tetragonal strain the orbital ordering is of ferrotype and the energy surface corresponds with a Mexican hat. On the other hand, if $\eta_\Gamma = 0$, the antiferro-ordering angle is

$$\tan\varphi_a = \frac{2F}{\Delta}Q_R, \tag{33}$$

which, when Q_R is small, involves a linear mixing between Γ and R wave functions, typical of a pseudo-Jahn-Teller effect, as confirmed inspecting the resulting quadratic energy surface.

The main physical ingredient that establishes a difference between our model and other orbital ordering descriptions [10–14,16] is the existence of a gap due to the mixing of E wave functions at Γ and R. This gap enforces Bloch's theorem and prevents broken symmetry solutions. In Fig. 6 we show the difference between a gapless model [16] (dashed lines) and our pseudo-Jahn-Teller model when the orthorhombic distortion $Q_{R\varepsilon}$ increases. We can see that in the gapless model and close to cubic symmetry [the central point in the polar plot Fig. 6(b)], φ_1 and φ_2 angles display a $180°$ difference, while according to Bloch's theorem, they should approach the center from the same direction. This is precisely what is observed in our gapped pseudo-Jahn-Teller model (solid lines), whose
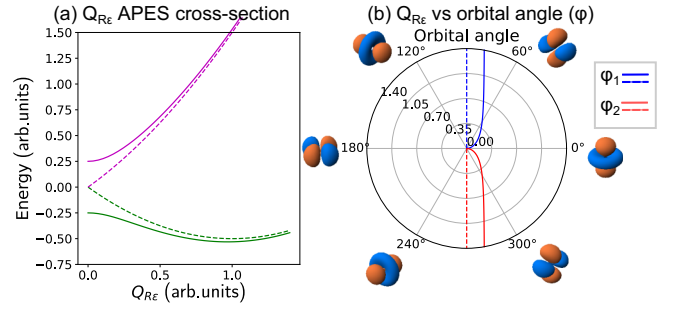

FIG. 6. Comparison of our combined Jahn-Teller–pseudo-Jahn-Teller model (solid lines) with a gapless electron-vibration orbital ordering model (dashed lines). In (a) we show the energy cross-section of both models with the $Q_{R\varepsilon}$ coordinate, where the gap at $Q_{R\varepsilon} = 0$ can be clearly seen. In (b) we represent the orbital angles at center 1 (blue) and 2 (red) in a polar plot as we increase $Q_{R\varepsilon}$ (radial coordinate).

prediction of orbital angles differs from gapless models for all values of $Q_{R\varepsilon}$. Moreover, current orbital ordering models do not take into account the strain mode η_Γ whose energy contribution increases the gap and further hinders the antiferrotype ordering of the orbitals.

As a final remark in this section, we would like to stress that the model above neglects magnetism, a major factor in many orbital-ordering models [10–13]. Our DFT simulations in Sec. IV A, in agreement with other calculations carried out by us [17,39] and other groups [18], show that, while superexchange influences the quantitative value of the orbital angles, its real effect is much smaller than that of the structure distortions considered in the previous model. Moreover, traditional orbital ordering models rely on expressing the energy through orbital-orbital interactions in the form of Heisenberg-like Hamiltonians that favor either ferro- or antiferrotype orderings. In contrast, the model presented here contains two-types of interactions (ferro and antiferro) that have similar strength, cooperate, and cannot be expressed through effective close-neighbor relations, since the presence of each kind of interconnection is associated with independent distortions.

III. COMPUTATIONAL DETAILS

First-principles DFT calculations were used to support our many-body model in crystals containing unpaired electrons in locally degenerate states. The calculations of the periodic structure were performed using the CRYSTAL17 and VASP codes. The Vienna *Ab initio* Simulation Package (VASP) [43,44] employs a set of plane waves to express the Bloch orbitals. To scrutinize the interplay between electronic and vibrational degrees of freedom and its impact on the magnetic state of the system, the electron correlation requires treatment beyond the conventional DFT level. Liechtenstein's LDA $+ U$ description [45] (we also used [45] $U = 7.5$ eV and $J = 0.9$ eV for $KCuF_3$), and the HSE06 functional [46], incorporating 25% Hartree-Fock (HF) exchange, were employed over the standard Perdew-Burke-Ernzerhof (PBE) generalized gradient approximation (GGA). This approach enhances the depiction of these systems as insulators by rectifying the self-interaction error.

To accommodate all the geometry distortions and magnetic states, the simulations of the cubic Pm-$3m$ and tetragonal $P4/mmm$ of $KCuF_3$ are carried out in a $\sqrt{2} \times \sqrt{2} \times 2$ supercell that is compatible with the one used to describe the fully distorted ground state with $I4/mcm$ symmetry. On the other hand, the CuO calculations are carried out in a $2 \times 1 \times 2$ monoclinic $C2/c$ supercell, while for the $CuCl_2$ calculations a $\sqrt{2} \times \sqrt{2} \times 1$ rectangular $C2/m$ supercell is used.

The convergence criterion for the electronic self-consistent loop was established at 1×10^{-6} eV, and atomic positions underwent relaxation, employing the conjugate gradient algorithm, until forces per atom converged to less than 0.03 eV/Å. Initial orbital occupancies were determined by a Gaussian smearing with $\sigma = 0.05$. The Brillouin zone was sampled through a $2 \times 2 \times 2$ k-point mesh for $KCuF_3$ while a $4 \times 4 \times 2$ was used for CuO and $4 \times 4 \times 1$ for $CuCl_2$. All of them are centered at the Γ point. Valence electrons were represented by a plane-wave basis set with a 520 eV energy cutoff, while core electrons were described using the projector augmented wave method (PAW) [47] along with pseudopotentials [48]. The valence electrons for the PAW potentials are 17, 12, and 9 for the Cu, Zn, and K cations, respectively, 7 for F and Cl, and 6 for O.

To study the vibrational properties of the system while quenching vibronic coupling, the Cu^{2+} cation was replaced by the closed-shell Zn^{2+} cation. Phonon bands and information regarding frequencies and displacements associated with normal modes, required for obtaining projections over specific atomic movements, were computed using the PYTHON tool PHONOPY [49,50], with VASP as a calculator at the PBE level of theory. To account for LO-TO splitting near the Γ-point, the nonanalytical term described in Refs. [51,52] was incorporated into the dynamical matrix. The supercells employed to compute the forces used to build the dynamical matrix are $4 \times 4 \times 4$ for $KZnF_3$, $5 \times 5 \times 5$ for ZnO, and $4 \times 4 \times 1$ for $ZnCl_2$. The 3D representation of the spin density, derived from VASP calculations, was extracted from the CHGCAR file using the Python tool VASPKIT [53] and visualized using the graphical tool VESTA [54].

For the sake of comparison, all calculations were performed simultaneously using the CRYSTAL17 package [55,56]. In this code, crystalline orbitals are expanded as a linear combination of Bloch functions, expressed in terms of local functions. These local functions are defined using atom-centered Gaussian-type functions, directly taken from the CRYSTAL website [57].

Various hybrid functionals were employed in these calculations, including B1WC [58] (containing 16% of exact Hartree-Fock exchange), PW1PW [59] (20% of HF exchange), HSE06 [46] (25% of HF exchange), and PBE0 [60] (25% of HF exchange). We verified the consistency of the results with the increasing percentages of HF exchange. High-quality triple-ζ polarized basis sets, developed by Peintinger *et al.* [57,61], were used in the calculations.

For the integration over the first Brillouin zone, a dense $8 \times 8 \times 8$ grid was employed. TOLINTEG parameters for real-space integrals of the electronic density were fixed to 9, 9, 9, 9, and 18. The convergence criterion for the energy was set to 10^{-8} Hartree. To analyze the orbital ordering in $KCuF_3$, the charge and spin densities were calculated by means of Mulliken population analysis. Our results with hybrid functionals match all available geometry data (lattice parameters, atom-atom distances) within 1% of the experimental values.

IV. RESULTS OF DFT SIMULATIONS

In this section, we will discuss our main DFT results and compare them with the predictions of the model presented in Sec. II. We will first focus on $KCuF_3$ discussing both the energy surface and the orbital ordering for different magnetic states. At the end of this section, we will briefly present systematical errors that appear in the simulations of periodic systems with lattices of active Jahn-Teller sites due to the limitations of one-electron Kohn-Sham DFT (or Hartree-Fock). We will then show how CuO and bidimensional $CuCl_2$, two systems that display important structural differences with $KCuF_3$, behave in a completely similar way to this system when observed through the prism of the model.

A. Perovskite lattice: $KCuF_3$

The most common phase of $KCuF_3$, usually called A-type, displays [62] a three-dimensional alternating pattern of in-plane long ($R_l = 2.296$ Å)/short ($R_s = 1.848$ Å) fluorine-copper bonds in the x/y directions (the axial bond lengths in the z-direction are $R_{ax} = 1.963$ Å) where the measured magnetic state is antiferromagnetic-A (AF-A) (ferromagnetic in the xy-plane and antiferromagnetic between planes). In the literature [4,28,63], this antiferrodistortive pattern has been understood as the main distortion of the system and coming from the condensation of the $Q_{R\varepsilon}$ mode. However, little attention (there are a few exceptions, like the interesting work by Kataoka [64], Marianetti [65], and recent calculations by Pascale *et al.* [66]) has been paid to the global compression that the whole lattice displays and that can be measured, for example, by comparing the in-plane (xy) Cu-Cu distance, $d = 4.144$ Å, with the out-of-plane one, $d = 3.926$ Å, that corresponds with a negative $\eta_{\Gamma\theta}$. DFT simulations, using different codes, basis, and methods, correctly predict the magnetic state and the geometry, with typical errors in distances below 1% for hybrid functionals. Thus, we can conclude that DFT methods are reliable to predict the low-symmetry equilibrium phase and its associated properties as fully supported by many computational works in the literature [18,28,63].

Performing calculations close to the cubic high-symmetry configuration, however, is not so simple. Due to the closeness of the partially filled e_g-bands, calculations often predict a metallic state that is quite high in energy with respect to the insulating state. This has been reported by other authors like Varignon [63], and its avoidance often requires the use of special initial states/shifting of levels [66] before the SCF cycles. Moreover, in a Jahn-Teller system the cubic symmetry is not a critical point of the energy surface, due to the presence of the conical intersection, i.e., there exist a nonzero force, which makes optimizing the geometry while retaining cubic symmetry difficult. Here we have used, as a cubic starting point, the geometry of the parent system of $KCuF_3$, the rigorously cubic lattice $KZnF_3$. From that cubic configuration we have followed the individual $\eta_{\Gamma\theta}$ and $Q_{R\varepsilon}$ modes to determine
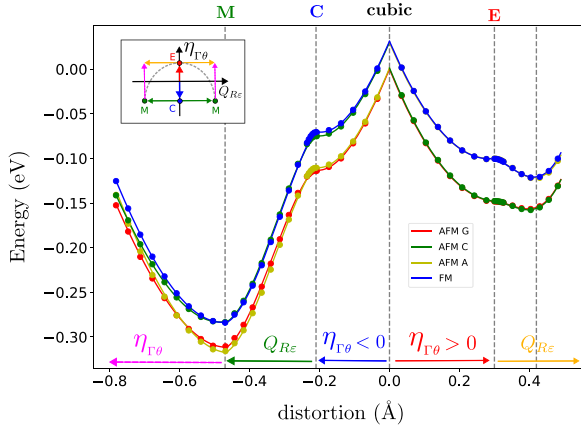
FIG. 7. DFT-calculated energy surface of KCuF$_3$ as the system distorts from cubic (*Pm-3m*) symmetry to tetragonal *P4/mmm* compressed (C) and elongated (E) geometries using the $\eta_{\Gamma\theta}$ mode and along the orthorhombic, $Q_{R\varepsilon}$, towards tetragonal *I4/mcm* symmetry. The different paths are sketched in the inset and are indicated at the bottom of the figure by colored arrows. Red, green, yellow, and blue lines denote the energy surface for antiferromagnetic G, C, A, and ferromagnetic, respectively.

FIG. 8. DFT-calculated energy surface of KCuF$_3$ following the $Q_{R\theta}$ starting off the elongated (E) geometry. A state crossing can be seen at $Q_{R\theta} \approx 0.3$ Å where the spin-density for the unpaired holes (see the insets) goes from $d_{x^2-y^2}$ to an alternating $d_{x^2-y^2}/d_{z^2}$ in a deep minimum where the lowest magnetic state is AF-C. The color of the lines is the same as that in Fig. 7, and the blue/yellow color of the electron density indicates spin-up/spin-down, respectively.

the energy surface and the shape of the wave function that characterizes the orbital ordering.

We start by looking at the effect of following the compression/elongation of the whole lattice, the $\eta_{\Gamma\theta}$ strain mode, shown in Fig. 7, a geometry that is described by the *P4/mmm* space group. We observe that this energy surface reflects the usual characteristics of an $E_g \otimes e_g$ Jahn-Teller effect: (i) At the cubic phase we observe a conical intersection of the two branches of an E_g state. Analysis of the wave function in each of these branches shows ferrotype orbital ordering, as shown in Fig. 9(b), which is fully consistent with Bloch's theorem as we get closer to the cubic geometry. (ii) The energies of elongated and compressed phases (C and E in Fig. 7) are different, and this difference quantifies the warping of the Mexican hat [2,19] described by Eq. (12). The elongated geometry is slightly favored as it occurred in the KZnF$_3$:Cu^{2+} impurity center [21]. (iii) Even though the critical points shown are found by distorting the lattice along the *z*-axis, fully equivalent distortions can be found distorting the lattice along *x*- or *y*-axes, which is consistent with the initial cubic symmetry. (iv) The Jahn-Teller energy is a sizable part of the global stabilization energy, 140–160 meV, depending on the magnetic state and the direction of distortion. Quite importantly, we observe that this energy is quite similar among all different magnetic states [ferromagnetic (FM), antiferromagnetic A (AF-A), antiferromagnetic C (AF-C), and antiferromagnetic G (AF-G)] that appear as almost parallel lines in Fig. 7.

After reaching the elongated and compressed configurations, our model predicts that the system can further distort along the *R*-modes. The global minimum can be found by following $Q_{R\varepsilon}$. However, we observe two very different behaviors depending on whether we start from the compressed (C) or the elongated (E) geometries. On the one hand, starting on the elongated geometry, we observe that this configuration is, in fact, a transition state with a negative force constant
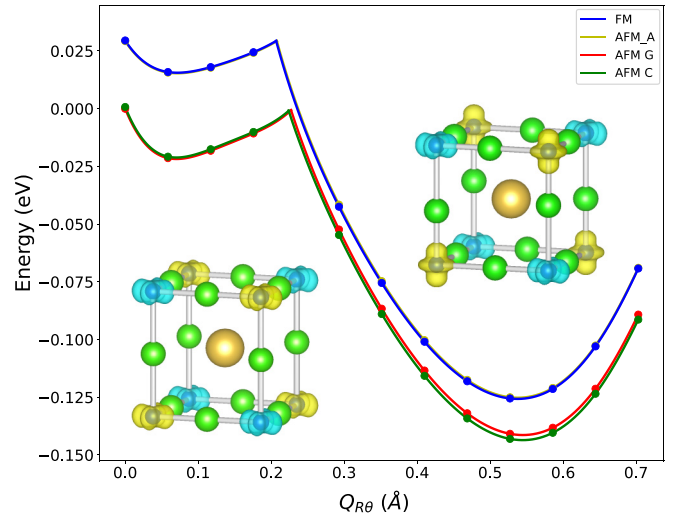
(instead of a linear stabilization energy associated with a Jahn-Teller effect; compare with the case of CuCl$_2$ later). However, the distortion and stabilization energy (≈ 20 meV) associated with this instability are quite modest (yellow path in Fig. 7). On the other hand, starting from the compressed geometry, we find a large stabilization energy (≈ 210 meV) and distortion. The contrast of starting from either the E or C transition states reflects the ease of deforming the Cu-F-Cu bond in the plane when the Cu-Cu distance is large (C) or its difficulty when it is small (E). This change in the force constant is a key characteristic of the pseudo-Jahn-Teller effect [2] that describes the changes in bonding occurring when a distortion is introduced in the system. In this model, the force constant contains two contributions: a primary force constant K_0 that reflects the electronic density optimized for the initial geometry and that opposes distortion, and the vibronic force constant K_v that
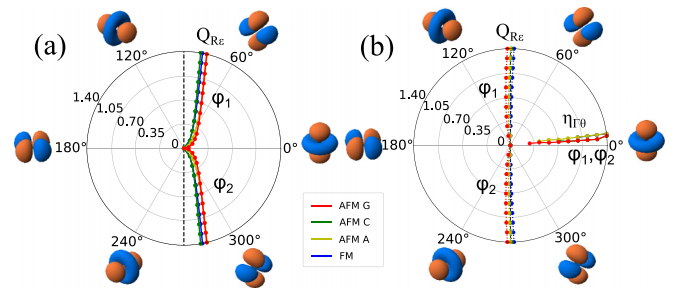

FIG. 9. DFT diagram showing the orbital ordering in KCuF$_3$ for the various magnetic orders. In (a) we show the change in φ_1 and φ_2 following $Q_{R\varepsilon}$ for nonzero η_Γ (segment C-M in 7). Compare with the model in Fig. 6. In (b) we show the equivalent change following $\eta_{\Gamma\theta}$ (cubic-E segment in Fig. 7 with ferro-ordering) compared to the symmetry broken solutions (dashed lines) ($Q_{R\varepsilon}$ mode) (see Fig. 10).

describes the effect of the change of the wave function to adapt to the new geometry. In this case, the main difference in the wave function between the ground and excited states is the phase in different neighboring centers, and the orthorhombic motion is associated with cooperation between sites [67]. In our model, the anharmonic strain-phonon coupling, Eq. (13), increases or reduces the elastic pseudo-Jahn-Teller primary force constant to account for the larger or smaller Cu-ligand distances. Meanwhile K_v is associated with the vibronic constant F associated with the local Jahn-Teller in each of the centers and the separation between many-body states Δ.

Another prediction of our model, associated with the coupling between strain and phonon modes, is the existence of minima on the elongated side of the energy surface ($\eta_{\Gamma\theta} > 0$), but instead of distorting along $Q_{R\varepsilon}$, the distortion is along $Q_{R\theta}$. Some orbital-ordering models based on electron-phonon coupling [16] show orbital patterns that are consistent with this kind of distortion. The energy surface obtained with hybrid functionals and starting from the elongated transition state is shown in Fig. 8. There we can see how the ground state of the system crosses from the wave function associated with a ferrotype state at E to an antiferrotype ($d_{z^2}/d_{x^2-y^2}$) orbital order associated with alternating elongated/compressed CuF_6^{4-} complexes along the z-axis. A full geometry optimization on this kind of geometry leads to an AF-C magnetic configuration that is only 25.5 meV above the AF-A global minimum. Thus, we have seen that the system presents two kinds of minima, one that has been extensively reported in the literature [4,18,28,63] and is associated with the antiferrodistortive $Q_{R\varepsilon}$ mode, and here we show another that is associated with the $Q_{R\theta}$ mode. The key distinction between both is that the one associated with $Q_{R\varepsilon}$ is *compressed in the plane* ($\eta_{\Gamma\theta} < 0$) while the one associated with $Q_{R\theta}$ is *elongated in the plane* [d(Cu-Cu)(x/y) = 4.04 Å, d(Cu-Cu)(z) = 4.16 Å]. Experimentally, stabilization of the second phase could be achieved by growing $KCuF_3$ (or another similar lattice like $KCrF_3$) on a substrate with a relatively small in-plane lattice parameter.

In Figs. 9(a) and 9(b) we show polar plots where the phase represents the orbital angles, φ_1 and φ_2, while the radial coordinates represent some of the distortions presented in Fig. 7. Let us first discuss [Fig. 9(a)] the orbital ordering when following the antiferrodistortive mode in the C → M segment of Fig. 7. This leads to alternating $x^2 - z^2/y^2 - z^2$ functions typical [10–14] of orbital-ordering models in $KCuF_3$. The first thing that we can observe is that the plotted line for φ_1 and φ_2 matches nicely the one in our model (solid lines in Fig. 6). Second, we should note that the orbitals are not pure $x^2 - z^2$ or $y^2 - z^2$, which are characteristic of *tetragonal* symmetry. This is a reasonable result since the local symmetry at the CuF_6 centers following this mode is *orthorhombic*. Third, we note that while φ_1 and φ_2 display antiferrodistortive orbital-ordering as they diverge for finite values of $Q_{R\varepsilon}$, they merge and approach the high-symmetry configuration (the center of the polar plot) from the same direction, i.e., the order becomes ferrodistortive, $\varphi_1 = \varphi_2$, as demanded by Bloch's theorem. Another important feature of our result is that the orbital angles φ_1 and φ_2 change with $Q_{R\varepsilon}$, something that does not happen in Jahn-Teller problems [2,19]. The angle change represents a *variation* of the wave function, the mixture of the wave functions at Γ and R, a modification in covalency that

is a fingerprint of the pseudo-Jahn-Teller effect [2], which is not present in the pure Jahn-Teller effect [see Eqs. (1)–(4)]. We can observe now in Fig. 9(b) what happens when we move from the cubic to the elongated geometries ($\eta_{\Gamma\theta}$ coordinate), cubic → E segment of Fig. 7, that we associated in Sec. II with a pure Jahn-Teller effect. As the $\eta_{\Gamma\theta}$ coordinate is followed, we see that both φ_1 and φ_2 match each other and come out radially from the center without changing their values, which confirms that this distortion mode corresponds, as expected, with a plain Jahn-Teller effect. Finally, we note that our results (Fig. 9) are, except for small numerical differences, independent of the magnetic state studied. Our DFT results show that magnetism plays a minimal role in the orbital ordering that is determined by the geometry, a result that has been stressed before by several authors [17,18,39].

1. Symmetry-breaking

We would like to discuss now what happens in DFT calculations when the cubic geometry is approached using either the mode $\eta_{\Gamma\theta}$ or $Q_{R\varepsilon}$. The energy surfaces are shown in Fig. 10 and the orbital angles in Fig. 9(b). In these plots the solid/dashed lines correspond, respectively, with $\eta_{\Gamma\theta}$ and $Q_{R\varepsilon}$. The curves for the strain mode are the same as those in the segments cubic → C and cubic → E in Fig. 7 and they become degenerate at $\eta_{\Gamma\theta} = 0$ to form an E-state. Similarly, the curves for the phonon mode meet in the cubic geometry to produce an E-state. However, the energies for these two E states are not the same. We have checked that this result appears consistently through a large variety of methods, including localized basis sets (CRYSTAL [55] and SIESTA [68] codes), plane waves (VASP code [43,44]), hybrid or LDA + U functionals, and several ways of generating the initial guess for the density matrix.

Analysis of the wave function and spin polarization of each of these solutions (see the insets in Fig. 10) shows that the orbital ordering when following the strain mode is of ferrotype while that corresponding with the R-phonon mode is of antiferrotype. Observing the variation of the orbital angles in Fig. 9(b), we see that the angles of both configurations come out radially, i.e., without the orbital angles changing, as characteristic of a Jahn-Teller situation. However, as discussed in the theory section (Sec. II), an antiferrotype orbital ordering is not possible for the cubic geometry as it violates Bloch's theorem. This computational problem comes from using a supercell and the relatively simple wave function typical of the Kohn-Sham DFT that can only account for single configurations (in the quantum chemistry sense; see, e.g., [69,70]). In simpler terms, the Kohn-Sham solution following the $Q_{R\varepsilon}$ mode close to cubic symmetry is *symmetry-broken* [70–72], i.e., it cannot fulfill symmetry requirements like Bloch's theorem, and it provides solutions, as illustrated by the spin densities in Fig. 10 that mix the translational character of Γ and R wave functions that is forbidden at the cubic symmetry. Thus, although the solutions for DFT are correct for fully relaxed low-symmetry configurations, as stressed by Varignon *et al.* [73], as we get closer to high symmetry, supercell solutions may not be adequate and symmetry-broken solutions may appear. These may be difficult to detect and appear to be present in much of the literature [28,29] of
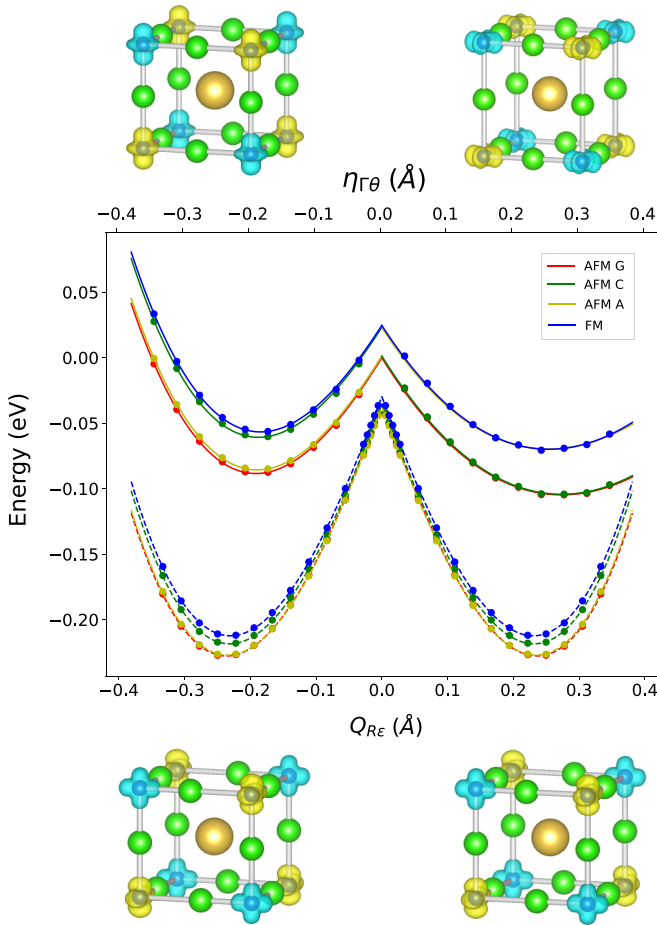
FIG. 10. DFT-calculated energy surface of KCuF$_3$ following the $Q_{R\epsilon}$ phonon-mode (dashed lines, lower axis) and the $\eta_{\Gamma\theta}$ strain-mode (solid lines, upper axis) starting off the elongated (E) geometry. It can be seen that these lines do not meet at cubic symmetry, as expected. The reason is that the calculations following $Q_{R\epsilon}$ converge to a symmetry-broken state (see spin-densities in the inset) where the wave function changes from site to site, something forbidden at cubic geometries by Bloch's theorem while the calculations for $\eta_{\Gamma\theta}$ are compliant with symmetry (see the inset). The color of the lines is the same as that in Fig. 7.

DFT/Hartree-Fock calculations of these systems, and they may hamper the correct interpretation of the vibronic energy of the observed phenomena or calculating high-symmetry transition states between low-symmetry minima. However, we would like to stress that these computational problems do not affect the low-symmetry, *observable* parts of the energy surface, and so much of the predictions carried out earlier are still valid, just not those involving the origin of the vibronic problem.

Going back to Fig. 10, we can now further observe that the curve for $Q_{R\epsilon}$ is symmetrical with respect to $Q_{R\epsilon} = 0$, something that is not present in usual Jahn-Teller problems where the elongated/compressed minima appear for different energies, giving rise to the warping of the Mexican hat and the barrier for the pseudorotation [2,19,20]. These facts further stress that the dashed lines in Fig. 10 do not represent proper physical behavior and, in fact, reflect the pseudo-Jahn-Teller
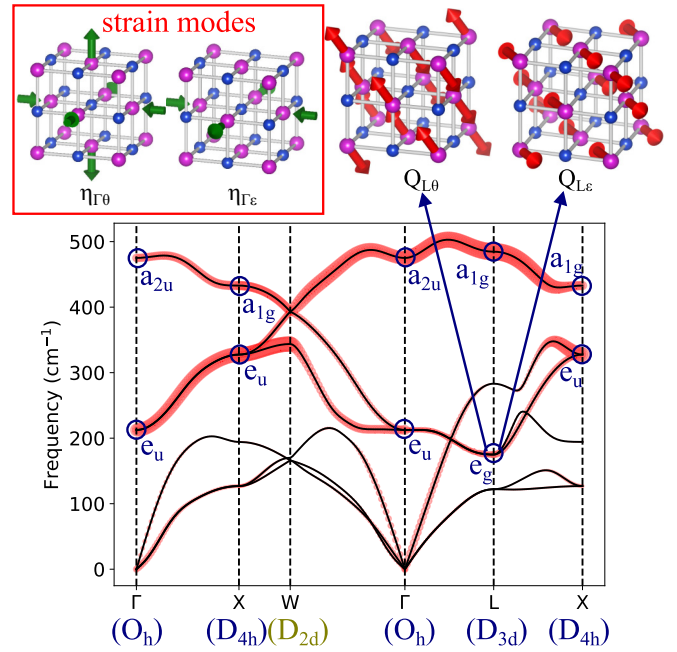

FIG. 11. DFT phonon bands projected on O. Reciprocal space points with inversion are indicated in blue while those without are labeled in yellow. The distortions of the e_g-symmetry modes (both strain and phonon) are represented at the top of the figure. Cu and O ions are represented, respectively, by blue and magenta spheres.

(gapped) vibronic coupling behind $Q_{R\epsilon}$, as discussed in our model of Sec. II.

Up to now we have confined our calculations to KCuF$_3$ in order to show the different aspects (multiple minima, coupling to strains, new aspects of orbital ordering) of vibronic coupling in crystals presented in our model. Over the next two sections, we will discuss how the same model is applicable to systems with quite different parent structures (rocksalt and a trigonal bidimensional lattices) instead of perovskite, as discussed so far.

B. Rocksalt lattice: CuO

Another interesting problem where interconnected octahedral Cu^{2+} complexes appear is the CuO lattice, which, experimentally, belongs to the monoclinic $C2/c$ space group. We take the high-symmetry phase of CuO as that of ZnO, a rocksalt structure (Fm-$3m$ group) where, contrary to the previous perovskite example, the octahedra are joined along the edges instead of the vertexes. Obviously, the phonon modes of ZnO, shown in Fig. 11, are quite different from those of KZnF$_3$. However, our criterion for looking for active vibronic modes is the same as for KZnF$_3$, as we need them to couple to an E_g electronic state. From the point of view of the strain modes of this crystal, we have the $\eta_{\Gamma\theta}$ and $\eta_{\Gamma\varepsilon}$ modes represented in Fig. 11, which behave in a completely equivalent manner to those in KCuF$_3$. However, looking at phonon modes, the only point in the reciprocal space of a rocksalt crystal that displays cubic symmetry (O_h) is Γ. At this point, the mainly oxygen modes are odd (a_{2u}, e_u) and cannot couple to the even E_g electronic state. Of all the other points with inversion symmetry, the only point with an e_g
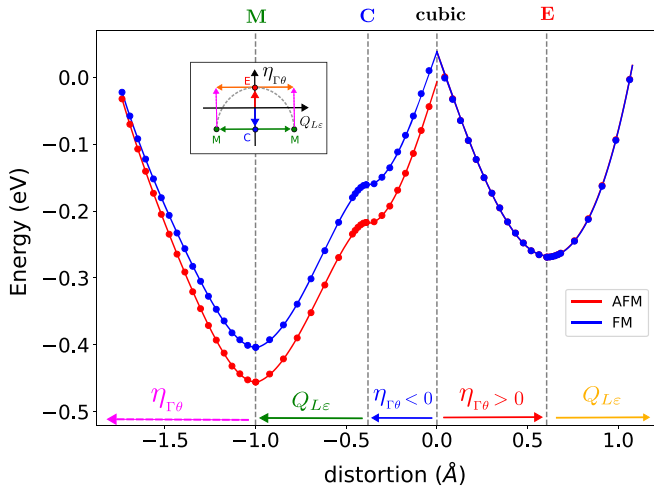
FIG. 12. DFT-calculated energy surface of CuO as the system distorts from cubic (Fm-$3m$) symmetry to $I4/mmm$ tetragonal compressed (C) and elongated (E) geometries using the $\eta_{\Gamma\theta}$ mode and, afterwards, along the $Q_{L\varepsilon}$ mode towards monoclinic $C2/c$ symmetry. The different paths are sketched in the inset and are indicated at the bottom of the figure by colored arrows. Red and blue lines denote the energy surface for antiferromagnetic and ferromagnetic states, respectively.

mode is L ($\frac{1}{2}, \frac{1}{2}, \frac{1}{2}$), where we find antiferrodistortive modes $Q_{L\theta}$ and $Q_{L\varepsilon}$ that fulfill the role of $Q_{R\theta}$ and $Q_{R\varepsilon}$ in KCuF₃. It is important to note that these modes at R do not display a pure stretching character like those at R for KZnF₃, and they distort the structure towards lower symmetry (monoclinic instead of tetragonal). Similar conclusions were reached by Grochala *et al.* [74] although with a symmetry-broken solution. With respect to the magnetic states, we consider the ferromagnetic and the antiferromagnetic state present in the experimental structure [75].

Let us now discuss the energy surface analyzing, as we did for KCuF₃ in Fig. 7, the distortion along $\eta_{\Gamma\theta}$ followed by $Q_{L\varepsilon}$. This is shown in Fig. 12, where we can see the strong qualitative resemblance with Fig. 7. We can observe that the curves leading to the elongated (E) and (C) transition states are asymmetric, as characteristic of a warped Mexican hat, and lead to tetragonal geometry ($I4/mmm$ space group). The stabilization energy and distortions in the CuO lattice, involving Jahn-Teller energies close to 250 meV, and local distortions involving changes of the Cu-O distance of 0.175 Å, are much larger than those in KCuF₃, involving energies of 150 meV and displacements of 0.08 Å, probably because distortions do not have a fully stretching character in the CuO case. From those tetragonally distorted reference points, we introduce the $Q_{L\varepsilon}$ distortion that further reduces the space group of the system to $C2/c$. As in the case of KCuF₃, we see that starting from the compressed and elongated geometries leads to very different results, but in this case the effect is further exaggerated due to the large distortions along $\eta_{\Gamma\theta}$. On the one hand, we see that following $Q_{L\varepsilon}$ from the elongated configuration (E) leads to a quadratic increase of energy. This means that the elongation of the complexes is so strong that the pseudo-Jahn-Teller effect is not strong enough to gain energy when moving the oxygen atom asymmetrically

between two copper ones following $Q_{L\varepsilon}$. In technical terms, this means that the anharmonic coupling term, Eq. (13), has increased the elastic force constant, K_0, above the vibronic contribution to the force constant, K_v [2]. On the other hand, we see that following $Q_{L\varepsilon}$ from the compressed configuration (C) reduces the energy quadratically, as is characteristic of a pseudo-Jahn-Teller effect. In this case, the $Q_{L\varepsilon}$ stabilization energy is ≈ 250 meV, slightly less than that gained through the Jahn-Teller effect along $\eta_{\Gamma\theta}$. This increased stabilization energy with respect to the elongated configuration is due to the enlarged Cu-O in-plane distance introduced by the tetragonal distortion, showing the importance of the coupling between these two modes.

In summary, we have seen that the treatment of the cooperative vibronic problem in CuO is completely analogous to the one in KCuF₃ where accounting for the interplay between strain ferrodistortive and phonon-based antiferrodistortive distortions is necessary to understand the complex energy surface.

C. 2D hexagonal: CuCl₂

Let us now move to trigonal CuCl₂ where, contrary to the previous cases, the experimental geometry indicates ferrodistortive ordering [76]. Here the high-symmetry configuration is not cubic as it belongs to the P-$3m1$ space group. This can be checked if all the Cu²⁺ ions are replaced by Zn²⁺ and a full optimization of the resulting ZnCl₂ crystal is carried out. While in nature the CuCl₂ crystal is formed by van der Waals bonded layers [76], here we have decided to center our attention on a single CuCl₂ layer, which is where the main vibronic interactions take place. This layer is formed by a middle plane containing Cu²⁺ ions creating a perfectly bidimensional, hexagonal lattice surrounded above and below by two hexagonal planes of Cl⁻ ions. The Cu²⁺ ion is situated inside a six-coordinates CuCl₆ complex that does not have octahedral (O_h) symmetry but a trigonal one (D_{3d}), resembling a flattened octahedron. This trigonal deformation does not break the degeneracy of the e_g shell of an octahedral complex, and the local electronic configuration is still e_g^3, just like in the previous cases of KCuF₃ and CuO. Again, we consider two magnetic states: the ferromagnetic one and an antiferromagnetic one. In the high-symmetry configuration, all antiferromagnetic states are frustrated, but this effect is quenched as the system distorts. We have chosen the antiferromagnetic state to be consistent with this reduction of symmetry.

Let us analyze the phonon diagram for the Pm-31 phase of ZnCl₂ shown in Fig. 13. We can observe that, among the high-symmetry points of the first Brillouin zone of ZnCl₂, we have points, Γ and M, that display inversion symmetry while K, whose little group is D_3, does not. The little group for M, C_{2h}, does not allow the presence of degenerate e-type irreps, while on Γ, whose little group is D_{3d}, we find an active e_g phonon mode. It is important to note that, contrary to the cases of KCuF₃ and CuO where the e_g phonon modes were located at the edge of the first Brillouin zone and gave rise to antiferrodistortive deformations of the lattice, in CuCl₂ the mode is centered at Γ and is ferrodistortive (all cells of the lattice will distort in the same way). Moreover, when
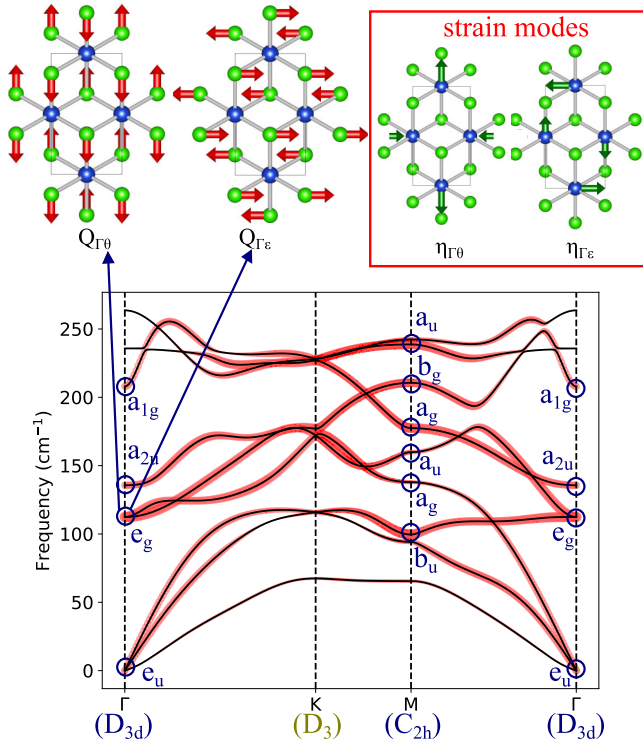
FIG. 13. DFT phonon bands projected on Cl. Reciprocal space points with inversion are indicated in blue, while those without are labeled in yellow. The distortions of the e_g-symmetry modes (both strain and phonon) are represented at the top of the figure.

FIG. 14. DFT-calculated energy surface of $CuCl_2$ as the system distorts from trigonal (P-$3m1$) symmetry to rectangular $C2/c$ compressed (C) (obtuse triangles) and elongated (E) (acute triangles) geometries using the $\eta_{\Gamma\theta}$ mode and, afterwards, along the $Q_{\Gamma\theta}$ mode towards $C2/c$ symmetry. The different paths are sketched in the inset and are indicated at the bottom of the figure by colored arrows. Red and blue lines denote the energy surface for antiferromagnetic and ferromagnetic states, respectively.

we consider the strain deformations, we find, as in previous cases, that there exist two distortion modes that transform according to the e_g-symmetry in D_{3d}. Note that while these modes elongate/compress the $CuCl_6$ somewhat, their main effect on the lattice is to transform equilateral Cl_3 triangles on the top/bottom Cl^--layers into obtuse (Cl-Cl-Cl angle 66.9°)/acute (Cl-Cl-Cl angle 54.4°) triangles, in a similar way to the Jahn-Teller deformation of triangular (H_3, Cu_3, . . .) molecules [2,19].

From the electron-phonon point of view, it is important to note that, since the vibrational mode is located at Γ, there is no need for a second electronic state at another point of the first Brillouin zone. That means that in $CuCl_2$ the pseudo-Jahn-Teller effect, responsible for the negative curvature in the energy surface along Q_R and Q_L modes in $KCuF_3$ and CuO, respectively, should be negligible and we expect to find a linear stabilization (proper Jahn-Teller effect) along both the strain and phonon modes. This is exactly what we observe in Fig. 14, which shows the results of our DFT simulations. Just as in Figs. 7 and 12, the distortion along η_Γ shows the presence of a conical intersection (linear descent of energy), however, instead of the quadratic curve when Q_R (or Q_L) modes are followed here, the Q_Γ mode leads to another linear decrease of the energy, consistent with the behavior of a multimode [2] Jahn-Teller problem. Given that all centers of the lattice distort in the same way, the orbital ordering in this lattice, independently of the magnetism, is of ferrotype and is fully consistent with the many-body model presented in Sec. II.
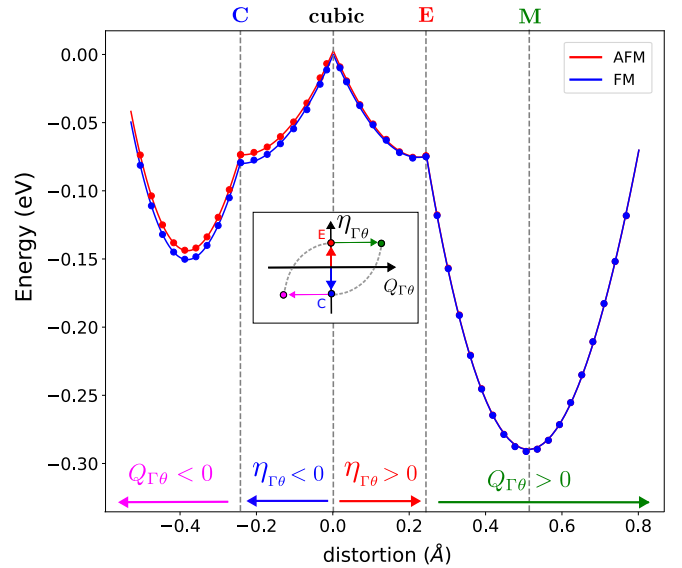
V. CONCLUSIONS

The presence of electronic degeneracy in solids is a very rich field of research that has been linked to many important phenomena in condensed-matter physics. However, the models usually employed to describe it, namely the cooperative Jahn-Teller effect and orbital-ordering, differed substantially from the well-known vibronic treatment of molecules and other localized systems like impurity centers. In this manuscript, we have shown that the usual formalism for the $E \otimes e$ Jahn-Teller problem can be used in solids. The main difference with molecules is the multielectronic/multimode nature of the the problem in solids. In contrast with previous approaches, we write the basic wave function for the vibronic Hamiltonian stressing the role played by the basic symmetry of crystals, i.e., translations and Bloch's theorem. Using this theorem, we can characterize the wave functions that lead to a many-body degenerate E_g state in a solid and show the correspondence of molecular and crystal problems. To deal with the distortions that couple to the degenerate state, we follow two paths: (i) we look for e_g vibrations in the phonon diagram, and (ii) we look for symmetrized strain distortions that transform like e_g. Our results show that, depending on where these vibrations are located in reciprocal space, the resulting distortion and orbital-ordering will be ferro- or antiferro-ordered. Moreover, our model shows that if the vibrations involved in the distortion of the system are at the edge of the first Brillouin zone, it is important to implicate a second E_g electronic state whose characteristic wave vector is different from the ground E_g state. The pseudo-Jahn-Teller mixing of these two states, that are separated by a gap, leads to antiferrotype orbital mixing. Our prediction differs qualitatively from previous orbital

ordering models because orbitals are not free to rotate due to the band structure of the cubic system, where electronic states at different points of reciprocal space have different energies. Another significant feature of our model is the importance of taking into account the coupling between the phonon and strain modes, that to our knowledge has only be previously discussed by Kataoka [64]. The main novelty is that our calculations show it to be, contrary to previous assumptions [4], cooperative and strongly influencing the energies of the system. In fact, our prediction is that the usual alternating $x^2 - z^2/y^2 - z^2$ antiferrotype orbital ordering associated with $KCuF_3$ and other similar crystals is the result of a compression on the xy plane of the lattice. We have found a close-by phase, associated with a similar vibronic problem where the lattice becomes elongated instead of compressed, where the orbital ordering alternates between $3z^2 - r^2$ and $x^2 - y^2$ localized functions. These phases could become the ground state of the system, for example, under the application of an in-plane compressive stress on the system, changing significantly the various properties of the crystal, like its magnetism. While in this work we have not dedicated much attention to the details of the magnetic structure, our calculations clearly show that the energy surfaces associated with the various magnetic states (FM, AF-A, AF-C, AF-G) are almost parallel, i.e., the energy scale of the electron-phonon coupling is much larger and dominates over the magnetic one. Also, detailed quantification of the wave function and orbital ordering shows that neither is greatly influenced by the magnetic state.

To finish, we would like to stress that the model here was applied to three quite different systems to show its generality, but each of these crystals displays very interesting characteristics and deserves particular attention in order to study in detail, for example, the interplay of the predicted new phases and the magnetic coupling. We hope that our work serves to clarify some of the fundamental aspects of the physics of these complex but very interesting materials.

ACKNOWLEDGMENTS

[1] H. A. Jahn and E. Teller, Proc. R. Soc. A **161**, 220 (1937).

[2] I. B. Bersuker, *The Jahn-Teller Effect* (Cambridge University Press, Cambridge, 2006).

[3] I. B. Bersuker and V. Z. Polinger, *Vibronic Interactions in Molecules and Crystals* (Springer-Verlag, Heidelberg, 1989).

[4] J. Kanamori, J. Appl. Phys. **31**, S14 (1960).

[5] M. D. Sturge, Sol. Stat. Phys. **20**, 91 (1969).

[6] G. A. Gehring and K. A. Gehring, Rep. Prog. Phys. **38**, 1 (1975).

[7] A. J. Millis, B. I. Shraiman, and R. Mueller, Phys. Rev. Lett. **77**, 175 (1996).

[8] H. Keller, A. Bussmann-Holder, and K. A. Müller, Mater. Today **11**, 38 (2008).

[9] V. Polinger, *The Jahn-Teller Effect: Fundamentals and Implications for Physics and Chemistry* (Springer, Heidelberg, 2009), pp. 685–725.

[10] D. I. Khomskii and S. V. Streltsov, Chem. Rev. **121**, 2992 (2021).

[11] K. I. Kugel' and D. I. Khomskiǐ, Sov. Phys. Usp. **25**, 231 (1982).

[12] K. I. Kugel' and D. I. Khomskiǐ, Zh. Eksp. Teor. Fiz. **64**, 1429 (1973) [Sov. Phys.-JETP **37**, 725 (1973)].

[13] Y. Tokura and N. Nagaosa, Science **288**, 462 (2000).

[14] J. van den Brink, Phys. Rev. Lett. **87**, 217202 (2001).

[15] I. Sánchez-Movellán, J. Moreno-Ceballos, P. García-Fernández, J. A. Aramburu, and M. Moreno, Chem. Eur. J. **27**, 13582 (2021).

[16] J. van den Brink, New J. Phys. **6**, 201 (2004).

[17] I. Sánchez-Movellán, M. Moreno, J. A. Aramburu-Zabala, and P. García-Fernández, J. Phys. Chem. C **127**, 8332 (2023).

[18] E. Pavarini, E. Koch, and A. I. Lichtenstein, Phys. Rev. Lett. **101**, 266405 (2008).

[19] P. García-Fernández, I. B. Bersuker, J. A. Aramburu, M. T. Barriuso, and M. Moreno, Phys. Rev. B **71**, 184117 (2005).

[20] P. García-Fernández and I. B. Bersuker, Phys. Rev. Lett. **106**, 246406 (2011).

[21] J. A. Aramburu, P. García-Fernández, J. M. García-Lastra, and M. Moreno, J. Phys. Chem. C **121**, 5215 (2017).

[22] J. H. van Vleck, J. Chem. Phys. **7**, 72 (1939).

[23] I. B. Bersuker, J. Exptl. Theoret. Phys. (U.S.S.R.) **43**, 1315 (1962) [Sov. Phys. JETP **16**, 933 (1963)].

[24] I. B. Bersuker, Sov. Phys. JETP **17**, 836 (1963).

[25] P. García-Fernández, A. Trueba, M. T. Barriuso, J. A. Aramburu, and M. Moreno, Phys. Rev. Lett. **104**, 035901 (2010).

[26] F. S. Ham, in *Electron Paramagnetic Resonance*, edited by S. Geschwind (Springer, New York, 1972), pp. 1–120.

[27] V. Polinger, J. Mol. Struct. **838**, 13 (2007).

[28] M. D. Towler, R. Dovesi, and V. R. Saunders, Phys. Rev. B **52**, 10150 (1995).

[29] M. M. Schmitt, Y. Zhang, A. Mercy, and P. Ghosez, Phys. Rev. B **101**, 214304 (2020).

[30] W. Kohn, Phys. Rev. **133**, A171 (1964).

[31] R. M. Martin, L. Reining, and D. M. Ceperley, *Interacting Electrons: Theory and Computational Approaches* (Cambridge University Press, Cambridge, 2016).

[32] R. D. Shannon, Acta Cryst. A **32**, 751 (1976).

[33] M. Kataoka and J. Kanamori, J. Phys. Soc. Jpn. **32**, 113 (1972).

[34] M. T. Hutchings, E. J. Samuelsen, G. Shirane, and K. Hirakawa, Phys. Rev. **188**, 919 (1969).

[35] U. Öpik and M. H. M. Pryce, Proc. R. Soc. London Ser. A **238**, 425 (1957).

[36] J. S. Griffith, *The Theory of Transition-Metal Ions* (Cambridge University Press, Cambridge, 2009).

[37] S. Yoshida, H. Akamatsu, and K. Hayashi, Phys. Rev. Lett. **127**, 215701 (2021).

[38] M. S. Dresselhaus, G. Dresselhaus, and A. Jorio, *Group Theory: Applications to the Physics of Condensed Matter* (Springer, Heidelberg, 2008).

[39] I. Sánchez-Movellán, G. Santamaria-Fernandez, P. García-Fernández, J. A. Aramburu-Zabala, and M. Moreno, J. Phys. Chem. C **127**, 16695 (2023).

[40] R. Peierls, *More Surprises in Theoretical Physics* (Princeton University Press, Princeton, NJ, 1979).

[41] M. V. Berry, Proc. R. Soc. London Ser. A **392**, 45 (1984).

[42] H. Longuet-Higgins, U. Öpik, and M. H. M. Pryce, Proc. R. Soc. London Ser. A **244**, 1 (1958).

[43] G. Kresse and J. Hafner, Phys. Rev. B **49**, 14251 (1994).

[44] G. Kresse and J. Furthmüller, Phys. Rev. B **54**, 11169 (1996).

[45] A. I. Liechtenstein, V. I. Anisimov, and J. Zaanen, Phys. Rev. B **52**, R5467(R) (1995).

[46] J. Heyd, G. E. Scuseria, and M. Ernzerhof, J. Chem. Phys. **118**, 8207 (2003).

[47] P. E. Blöchl, Phys. Rev. B **50**, 17953 (1994).

[48] G. Kresse and D. Joubert, Phys. Rev. B **59**, 1758 (1999).

[49] A. Togo, L. Chaput, T. Tadano, and I. Tanaka, J. Phys.: Condens. Matter **35**, 353001 (2023).

[50] A. Togo, J. Phys. Soc. Jpn. **92**, 012001 (2023).

[51] X. Gonze, J.-C. Charlier, D. C. Allan, and M. P. Teter, Phys. Rev. B **50**, 13035(R) (1994).

[52] X. Gonze, Phys. Rev. B **55**, 10337 (1997).

[53] V. Wang, N. Xu, J.-C. Liu, G. Tang, and W.-T. Geng, Comput. Phys. Commun. **267**, 108033 (2021).

[54] K. Momma and F. Izumi, J. Appl. Crystallogr. **41**, 653 (2008).

[55] R. Dovesi, A. Erba, R. Orlando, C. M. Zicovich-Wilson, B. Civalleri, M. Rérat, S. Casassa, J. Baima, S. Salustro, and B. Kirtman, WIREs Comput. Molec. Sci. **8**, e1360 (2018).

[56] R. Dovesi, V. R. Saunders, C. Roetti, R. Orlando, C. M. Zicovich-Wilson, F. Pascale, B. Civalleri, K. Doll, N. M. Harrison, I. J. Bush, Ph. D'Arco, M. Llunel, M. Causà, Y. Noël, L. Maschio, A. Erba, M. Rérat, and S. Casassa, "Crystal17 user's manual" (2018).

[57] "CRYSTAL basis sets," https://www.crystal.unito.it/basis_sets.html, accessed: January 2023.

[58] D. I. Bilc, R. Orlando, R. Shaltaf, G. M. Rignanese, J. Iniguez, and P. Ghosez, Phys. Rev. B **77**, 165107 (2008).

[59] T. Bredow and A. R. Gerson, Phys. Rev. B **61**, 5194 (2000).

[60] C. Adamo and V. Barone, J. Chem. Phys **110**, 6158 (1999).

[61] M. F. Peintinger, D. V. Oliveira, and T. Bredow, J. Comput. Chem. **34**, 451 (2013).

[62] P. C. Burns, F. C. Hawthorne, A. M. Hofmeister, and S. L. Moret, Phys. Chem. Min. **23**, 141 (1996).

[63] J. Varignon, M. Bibes, and A. Zunger, Phys. Rev. Res. **1**, 033131 (2019).

[64] M. Kataoka, J. Phys. Soc. Jpn. **70**, 2353 (2001).

[65] C. A. Marianetti, D. Morgan, and G. Ceder, Phys. Rev. B **63**, 224304 (2001).

[66] F. Pascale, M. Pastore, K. Doll, and R. Dovesi, Chem. Phys. Lett. **836**, 141053 (2024).

[67] J. A. Aramburu, P. García-Fernández, N. R. Mathiesen, J. M. Garcia-Lastra, and M. Moreno, J. Phys. Chem. C **122**, 5071 (2018).

[68] J. M. Soler, E. Artacho, J. D. Gale, A. García, J. Junquera, P. Ordejón, and D. Sánchez-Portal, J. Phys.: Condens. Matter **14**, 2745 (2002).

[69] P. Sharma, J. J. Bao, D. G. Truhlar, and L. Gagliardi, Annu. Rev. Phys. Chem. **72**, 541 (2021).

[70] J. Paldus and A. Veillard, Mol. Phys. **35**, 445 (1978).

[71] P. Lykos and G. W. Pratt, Rev. Mod. Phys. **35**, 496 (1963).

[72] P. Löwdin, Adv. Chem. Phys. **14**, 283 (1969).

[73] J. Varignon, M. Bibes, and A. Zunger, Nat. Commun. **10**, 1658 (2019).

[74] M. Derzsi, P. Piekarz, and W. Grochala, Phys. Rev. Lett. **113**, 025505 (2014).

[75] G. Giovannetti, S. Kumar, A. Stroppa, J. van den Brink, S. Picozzi, and J. Lorenzana, Phys. Rev. Lett. **106**, 026401 (2011).

[76] M. Suzuki, I. S. Suzuki, C. R. Burr, D. G. Wiesler, N. Rosov, and K.-I. Koga, Phys. Rev. B **50**, 9188 (1994).